High-Fidelity Spin Qubit Shuttling via Large Spin-Orbit Interactions

Stefano Bosco[*,†], Ji Zou, and Daniel Loss

Department of Physics, University of Basel, Basel 4056, Switzerland

Shuttling spins with high fidelity is a key requirement to scale up semiconducting quantum computers, enabling qubit entanglement over large distances and favoring the integration of control electronics on-chip. To decouple the spin from the unavoidable charge noise, state-of-the-art spin shuttlers try to minimize the inhomogeneity of the Zeeman field. However, this decoupling is challenging in otherwise promising quantum computing platforms such as hole spin qubits in silicon and germanium, characterized by a large spin-orbit interaction and an electrically tunable qubit frequency. In this work, we show that, surprisingly, the large inhomogeneity of the Zeeman field stabilizes the coherence of a moving spin state, thus also enabling high-fidelity shuttling in these systems. We relate this enhancement in fidelity to the deterministic dynamics of the spin that filters out the dominant low-frequency contributions of the charge noise. By simulating several different scenarios and noise sources, we show that this is a robust phenomenon generally occurring at large field inhomogeneity. By appropriately adjusting the motion of the quantum dot, we also design realistic protocols enabling faster and more coherent spin shuttling. Our findings are generally applicable to a wide range of setups and could pave the way toward large-scale quantum processors.

I. INTRODUCTION

Spin qubits confined in silicon and germanium quantum dots are front-runners in the race toward large-scale quantum computers [1–15]. Their demonstrated compatibility with industry-level CMOS processing [15–18] and their high-temperature operations [18–22] make these systems ideal for scalability and cointegration with control electronics [23–28]. The small footprint of spin qubits, typically a few tens of nanometers, however, imposes demanding technological constraints for the classical hardware and requires dense multilayered architectures that add significant extra complexity to the process [29–32].

These constraints are significantly relaxed by introducing quantum links coupling distant spins that are placed micrometers apart [23]. This long-range connectivity can be achieved in various ways, including, for example, virtual couplings enabled by photons in superconducting cavities [33–49], Luttinger liquids [50–55], floating gates [56,57], and magnetic systems [58–63]. Correlated dissipative coupling emerging by appropriately engineering the spin coupling to a bosonic bath has also been proposed as a viable route to entangle distant qubits [64,65]. All these possibilities, however, require external components that are not straightforward to integrate into the conventional CMOS processes, therefore hindering the competitive advantage of spin qubits.

On the other hand, shuttling spins across the chip provides a viable and CMOS compatible way to link qubits in a sparse array [66–73]. The fidelity of this operation is determined by the noise that the spin experiences during shuttling and, in current devices, this noise is predominantly related to random fluctuations of the electrostatic environment. Because spin-orbit interactions (SOIs) directly couple the spin degree of freedom to these charge fluctuations, current experiments try to minimize the SOI to maximize the shuttling fidelity. This approach is challenging in hole-based spin qubits, whose predominant feature is their large SOIs [74–87]. The tunability of their SOIs enables sweet spots [88–95] where the SOI can be turned off; however, for shuttling operations, this optimization requires a demanding fine-tuning of the electrostatic potential over wide areas.

In this work, we show that, surprisingly, large SOIs and inhomogeneity of the Zeeman field can substantially *enhance* the shuttling fidelity. This improvement depends

---

*Corresponding author: s.bosco@tudelft.nl

†Current affiliation: QuTech and Kavli Institute of Nanoscience, Delft University of Technology, Lorentzweg 1, 2628 CJ Delft, Netherlands.

on the coherent dynamics imprinted by the SOI on the spin state. The spin moving in a large SOI field rotates quickly in a deterministic and controllable way and this motion provides an intrinsic dynamical decoupling, filtering out the dominant, low-frequency contribution of the noise, thus boosting shuttling fidelity. A similar SOI-induced decoupling appears in microwave-driven qubits [15,86] and is a continuous version of the typical instantaneously pulsed dynamical decoupling [96]. The high spin shuttling fidelities reached in our shuttling scheme are qualitatively independent of the type and spatial distribution of the noise sources, and can also be reached by moving spin in an inhomogeneous Zeeman field produced, for example, by varying g tensors [97,98] or micromagnets [1,67,99], opening up to effective SOI-driven improvements of the shuttling fidelity in electron spin qubits in silicon and germanium. Expanding on these ideas, we propose optimized protocols to leverage the SOI to further dynamically decouple the moving spin from the environment, rendering the shuttling faster and at the same time more coherent, and paving the way towards high-fidelity shuttling of hole spin qubits for the large-scale quantum processors.

This manuscript is organized as follows. In Sec. II, we introduce our general model describing spins shuttling in inhomogeneous SOI and Zeeman fields. Our theory captures the spin dynamics in a wide variety of setups, including the silicon and germanium spin qubits in fin field-effect transistors and heterostructures sketched in Fig. 1. In Sec. III, we specialize our discussion on inhomogeneous Zeeman fields only. This simple case provides a valuable intuitive understanding of the coherent and incoherent time evolution of the spin, and of the effect of different sources of noise. We expand the discussion in Sec. IV, by including an inhomogeneous SOI field, nicely describing realistic hole-based silicon and germanium devices. We show that a large effective SOI is beneficial to reduce the effect of noise during shuttling and, as proposed in Sec. V, it can be further leveraged in alternative shuttling schemes that dynamically decouple the spin from low-frequency noise. These protocols enable a faster motion of the spins and substantially boost the shuttling coherence of a wide range of materials and systems presenting large inhomogeneities of Zeeman fields.

II. THEORETICAL MODEL

In this work, we analyze spin qubits confined in moving quantum dots, as sketched in Fig. 1. The dynamic of the spin along the direction of motion (z direction) is well approximated by the effective one-dimensional Hamiltonian

$$H_{1D} = \frac{p^2}{2m} + \frac{m\omega_o^2}{2}[z - \bar{z}(t)]^2 - \{\mathbf{v}(z), p\} \cdot \boldsymbol{\sigma} + \frac{\hbar\tilde{\boldsymbol{\omega}}_B(z) \cdot \boldsymbol{\sigma}}{2}.$$
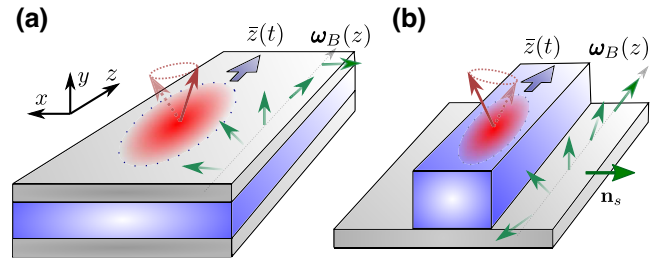
(1)

FIG. 1.   Sketch of our moving spin qubits. A particle confined in a quantum dot centered at the time-dependent position $\bar{z}(t)$ is shuttled along the z direction in a planar germanium heterostructure (a) or in a silicon fin field-effect transistor (b). During the motion, the spin of the particle (red arrows) precesses because of an inhomogeneous Zeeman field $\boldsymbol{\omega}_B(z)$ (green arrows), which can be caused by a space-dependent g tensor and magnetic field (a) or by a large spin-orbit interaction (SOI) with direction $\mathbf{n}_s$ (b). The fast SOI-induced dynamics of the spin filters out dangerous low-frequency noise and substantially boosts the fidelity of the spin shuttling.

This Hamiltonian describes a quantum dot with harmonic frequency ω_o and width $l = \sqrt{\hbar/m\omega_o}$, whose center of mass $\bar{z}(t)$ is shifted time dependently. This moving electric potential is experimentally implemented in conveyer-mode shuttling architectures [71–73]. In this work, we restrict ourselves to this type of shuttling; however, we expect that our results can also be generalized to bucket-brigade shuttling [66–70,100]. While Eq. (1) can capture the spin dynamics only of bucket-brigade experiments with large tunneling between quantum dots, we envision that the large inhomogeneity of Zeeman fields between dots can be leveraged to filter out low-frequency noise in general setups. During its motion, the spin experiences inhomogeneous spin-orbit and Zeeman fields, described by the vectors of spin-orbit velocities $\mathbf{v}(z)$ and Larmor frequencies $\tilde{\boldsymbol{\omega}}_B(z)$, respectively. We anticipate that the local Zeeman field of the nanostructure $\tilde{\boldsymbol{\omega}}_B(z)$ differs from the local qubit splitting $\boldsymbol{\omega}_B(z)$ by a correction arising from the confinement in the z direction [78,81–83]; see Eq. (2) below. Here, m is the effective mass along z, $p = -i\hbar\partial_z$ is the momentum operator in the direction of motion, $\boldsymbol{\sigma} = (\sigma_1, \sigma_2, \sigma_3)$ is the vector of Pauli matrices, and $\{a, b\} = (ab + ba)/2$ is the normalized anticommutator that guarantees the Hermiticity of H_{1D}.

Equation (1) generally captures the response of a wide variety of different setups, including those in Fig. 1. In particular, in this work, we focus primarily on hole spin qubit architectures, where the effective parameters originate from the mixture of heavy and light holes in the valence band caused by kinetic energy and strain and described by the Luttinger-Kohn and Bir-Pikus Hamiltonian. In one-dimensional hole channels in silicon and germanium, the SOI velocity $\mathbf{v}(z)$ is large, yielding experimentally measured SOI lengths $\lambda_s = \hbar/m|\mathbf{v}|$ of tens of

nanometers, comparable with the quantum dot width l [15,18,76–79]. In planar hole nanostructures, the SOI is generally smaller, although it can be enhanced by device engineering [81–85,101–104]. However, in these systems, the effective Zeeman field $\tilde{\boldsymbol{\omega}}_B^h(z) = \mu_B \hat{g}(z)\mathbf{B}/\hbar$ is also largely inhomogeneous because of the space-dependent and electrically tunable g tensor $\hat{g}(z)$, which also rotates the energetically preferred quantization axes at different locations when the externally applied magnetic field $\mathbf{B}$ is homogeneous [9,10,70,95,97,98]. We stress that our model also directly describes electron spin qubits moving in an inhomogeneous magnetic field provided, for example, by micromagnets [1–5]. In this case, similarly to planar hole heterostructures, the SOI $\mathbf{v}(z)$ is small, and the leading contribution to the spin dynamics is the inhomogeneous Zeeman field $\tilde{\boldsymbol{\omega}}_B^e(z) = \mu_B g \mathbf{B}(z)/\hbar$.

Throughout this work, we restrict ourselves to adiabatically moving quantum dots, and consider shuttling velocities that are slow compared to the orbital energy gap. The small corrections to our model arising from nonadiabaticity in the orbital degrees of freedom and an exact solution of a simple case where this condition is lifted are discussed in detail in Appendix A. We note that, for holes, this condition is $\hbar \partial_t \bar{z}/l \ll \hbar \omega_o \sim 1$ meV, while for electrons, in silicon and germanium this condition is more stringent and we require $\hbar \partial_t \bar{z}/l$ to be much smaller than the valley splitting. Large valley splittings commonly appear in silicon MOS and in strained heterostructures, reaching gaps of about 0.5 meV [105] and about 0.2 meV [106], respectively. In these systems, valley splitting is estimated to become relevant at fast shuttling velocities $\gtrsim 10$ m/s [73].

We emphasize that because $\hbar \omega_o \gg \hbar |\boldsymbol{\omega}_B(z)| \sim 0.01$ meV, in our adiabatically moving quantum dots, the dynamics of spin does not need to be adiabatic with respect to the Zeeman field and we anticipate that resonance processes with $\partial_t \bar{z}/l \sim |\boldsymbol{\omega}_B(z)|$ can further enhance the fidelity of spin shuttling; see Sec. V below.

Finally, in this work we restrict ourselves to setups where the inhomogeneity of the Zeeman field is deterministic and can be designed by either engineering the gate layout and electrostatic potentials in hole nanostructures [6,15,70,107], or by nanomagnets [99] in electronic systems. We foresee however that alternative protocols and possible improvement to shuttling fidelity could also be achieved for random Zeeman field inhomogeneities, in analogy to randomized dynamical decoupling schemes [108–110].

III. INHOMOGENEOUS ZEEMAN FIELD

A. Deterministic spin dynamics

We first focus on a spin moving in an inhomogeneous Zeeman field and neglect for the moment the effect of the SOI, i.e., $\mathbf{v} = 0$ in Hamiltonian H_{1D} of Eq. (1). This simple case captures the response of planar hole nanostructures and of electron spins moving in micromagnetic fields and shows how the spin dynamics during shuttling can filter out the relevant low-frequency noise sources.

Assuming that the confinement potential is strong compared to the local Zeeman field and restricting for now to shuttling processes that are adiabatic compared to both orbital and spin dynamics, i.e., $\omega_o \gg |\boldsymbol{\omega}_B(z)| \gg \partial_t \bar{z}/l$, we find by conventional time-dependent perturbation theory that the spin degree of freedom evolves according to the inhomogeneous Zeeman Hamiltonian

$$H_Z = \frac{\hbar}{2} \boldsymbol{\omega}_B[\bar{z}(t)] \cdot \boldsymbol{\sigma} \qquad (2)$$

with

$$\boldsymbol{\omega}_B[\bar{z}] = \int dz |\psi(z - \bar{z})|^2 \tilde{\boldsymbol{\omega}}_B(z);$$

see Appendix A for more details. The Zeeman energy of the quantum dot $\boldsymbol{\omega}_B$ contains quantitative corrections coming from the inhomogeneity of the field averaged over the charge density $|\psi(z - \bar{z})|^2 \approx e^{-(z-\bar{z})^2/l^2}/l\sqrt{\pi}$ of the particle. The adiabatic condition on the spin degrees of freedom constrains the shuttling velocity to be $\partial_t \bar{z} \ll \min |\boldsymbol{\omega}_B| l$. In current experiments, $|\boldsymbol{\omega}_B|/2\pi \sim 1$–10 GHz and $l \sim$ 10–100 nm, therefore constraining the shuttling velocities to $\lesssim 10$ m/s. We stress that these velocities are achievable with current hardware [71]. We relax this adiabatic condition in Sec. V below.

The time evolution of the spin generated by H_Z is well approximated by the adiabatic time-evolution operator

$$U_Z(t) \approx e^{-i\theta_B[\bar{z}(t)]\mathbf{n}_B[\bar{z}(t)]\cdot\boldsymbol{\sigma}/2} e^{-i\Phi_B(t)\sigma_3/2}. \qquad (3)$$

The first transformation $e^{-i\theta_B \mathbf{n}_B \cdot \boldsymbol{\sigma}/2}$ locally diagonalizes H_Z at position $\bar{z}$. The local angle $\theta_B[\bar{z}]$ and unit vector $\mathbf{n}_B[\bar{z}]$ are found by explicitly solving the equation $\boldsymbol{\omega}_B/|\boldsymbol{\omega}_B| = \hat{R}_B(\theta_B)\mathbf{n}_3$ for each value of $\bar{z}$. Here, $\mathbf{n}_3 = (0, 0, 1)$ and $\hat{R}_B(\theta_B)$ is an anticlockwise rotation matrix around axis $\mathbf{n}_B$ of angle θ_B; see Appendix B for more details and a general solution for vector $\mathbf{n}_B$ and angle θ_B. We conventionally choose the local angle θ_B to satisfy $\theta_B[\bar{z} = 0] = 0$ and $U_Z(t = 0) = 1$. Because of the adiabatic condition, we discard the negligible contribution to the Hamiltonian $-i\hbar e^{i\theta_B \mathbf{n}_B \cdot \boldsymbol{\sigma}/2} \partial_t e^{-i\theta_B \mathbf{n}_B \cdot \boldsymbol{\sigma}/2} \propto \partial_t \bar{z}/l \ll \min |\boldsymbol{\omega}_B|$ generated by the time dependence of θ_B and $\mathbf{n}_B$. Then the time evolution in this slowly locally rotated frame reduces to the spin-dependent phase accumulation given by the second exponential: $e^{-i\Phi_B(t)\sigma_3/2}$ with $\Phi_B(t) = \int_0^t |\boldsymbol{\omega}_B[\bar{z}(\tau)]| d\tau$. Nonadiabatic corrections compared to the Zeeman field arising from the discarded term $-i\hbar U_Z^\dagger \partial_t U_Z$ can prove beneficial for shuttling and are reintroduced and leveraged in Sec. V below.

Finally, we emphasize that nonadiabaticity compared to the orbital degree of freedom causes the additional

term $\hbar \partial_t \bar{z} \partial_{\bar{z}} \boldsymbol{\omega}_B \cdot \boldsymbol{\sigma} / 2\omega_o$ in H_Z in Eq. (2); see Appendix A. For a largely inhomogeneous Zeeman field, we can estimate $\partial_{\bar{z}} \boldsymbol{\omega}_B \sim \boldsymbol{\omega}_B / l$; thus, the additional corrections are suppressed by the small factor $\partial_t \bar{z} / \omega_o l \ll \partial_t \bar{z} / \min |\boldsymbol{\omega}_B| l \ll 1$.

B. Shuttling fidelity in a noisy environment

The unitary operator $U_Z(t)$ in Eq. (3) describes the coherent deterministic time evolution of the spin. Because U_Z can be characterized in experiments and can be compensated for or engineered to implement single-qubit gates, it does not influence the overall shuttling fidelity. However, during shuttling the spin also experiences random fluctuations in the environment that result in a loss of its coherence. At small shuttling velocities, the dominant contribution in a conveyer-mode shuttling process is estimated to be the variation of spin splitting caused by charge noise [73]. To describe this effect, we consider the noise Hamiltonian [88–90,96,111,112]

$$H_N = \frac{\mathbf{h}(t) \cdot \boldsymbol{\sigma}}{2}, \qquad (4)$$

where a stochastic, time-dependent vector $\mathbf{h}(t)$ couples to the spin. Physically, this vector originates from long-range fluctuations of the gate electric field (global noise sources) or from short-range atomistic defects (local noise sources) coupling to the spin by the effective SOI or hyperfine interactions. This Hamiltonian can also describe the effect of small random variations of the trajectory of the shuttled spin in the inhomogeneous field. A detailed comparison between local and global noise sources is delayed to Sec. III C. We anticipate that, while the microscopic origin of the noise quantitatively influences the shuttling fidelity, the coherent spin dynamics reduce the effect of the noise independently of the source, and for this reason, we focus first on the simpler case of global noise sources. The derivations for general cases are provided in Appendix C. We remark that in our model, we do not consider small possible modulations of noise sources by the potential applied to shuttle the quantum dot.

In the interaction picture, H_N is dressed by the time evolution of the spin as

$$H_N^I = U_Z^\dagger H_N U_Z = \frac{1}{2} \mathbf{h}(t) \cdot \hat{R}_Z(t) \boldsymbol{\sigma}, \qquad (5a)$$

$$\hat{R}_Z(t) = \hat{R}_{B(t)}[\theta_B(t)] \hat{R}_3[\Phi_B(t)]. \qquad (5b)$$

Here, $\hat{R}_Z$ is the combined rotation matrix generated by the adiabatic time-evolution operator U_Z in Eq. (3) and the notation $\hat{R}_{B(t)}[\theta_B(t)]$ emphasizes that $\hat{R}_B$ depends on time via its time-dependent rotation axis $\mathbf{n}_B(t)$ and angle $\theta_B(t)$; $\hat{R}_3$ is the rotation matrix about the local Zeeman

axis; see Appendix B for the explicit form. We note that in general the neglected nonadiabatic corrections $\propto \partial_t \bar{z}/l$ only weakly renormalize the direction and angle of matrix $\hat{R}_Z$; resonant cases where these corrections become nonnegligible are discussed in detail in Sec. V below. When noise is small, H_N generates the time-evolution operator $U_N \approx e^{-i \boldsymbol{\phi}_N(t) \cdot \boldsymbol{\sigma}/2}$, with the vector of random phases

$$\boldsymbol{\phi}_N(t) = \frac{1}{\hbar} \int_0^t d\tau \, \mathbf{h}(\tau) \hat{R}_Z(\tau). \qquad (6)$$

To quantify the error caused by the stochastic phase accumulation during shuttling, we introduce the fidelity of a single shuttling event

$$\mathcal{F} = \tfrac{1}{2} |\mathrm{Tr}(U_{\mathrm{id}}^\dagger U_{\mathrm{re}})| = \tfrac{1}{2} |\mathrm{Tr}(e^{-i \boldsymbol{\phi}_N \cdot \boldsymbol{\sigma}/2})| \qquad (7)$$

that measures the distance between the ideal (coherent) and real (noisy) operations $U_{\mathrm{id}} = U_Z$ and $U_{\mathrm{re}} = U_Z U_N$, respectively. The average shuttling fidelity $\bar{\mathcal{F}}$ is obtained by averaging $\mathcal{F}$ over the probability distribution of $\boldsymbol{\phi}_N$. Assuming a Gaussian-distributed noise [88,89,96,111, 112], we obtain

$$\bar{\mathcal{F}} = \int_{-\infty}^{\infty} d\boldsymbol{\phi}_N \frac{e^{-\boldsymbol{\phi}_N \cdot \hat{\Sigma}^{-1} \boldsymbol{\phi}_N / 2}}{\sqrt{8\pi^3 \det(\Sigma)}} \cos\left(\frac{\sqrt{\boldsymbol{\phi}_N \cdot \boldsymbol{\phi}_N}}{2} \right), \qquad (8)$$

where we have introduced the covariance matrix

$$\hat{\Sigma} = \frac{1}{2\pi\hbar^2} \int_{-\infty}^{\infty} d\omega \, S(\omega) \hat{F}(\omega, t) \qquad (9)$$

with determinant $\det(\Sigma)$; $S(\omega) = \int dt e^{i\omega t} \langle h(t)h(0) \rangle$ is the power spectral function of the noise, which, for simplicity, we have assumed to be isotropic and uncorrelated in space and spin directions, i.e., $\langle h_i(t)h_j(0) \rangle = \delta_{ij} \langle h(t)h(0) \rangle$. The generalization of Eq. (9) for noise sources that couple to the moving spin anisotropically [89,111,112] is straightforward and is provided in Appendix C. The matrix of filter functions [96]

$$\hat{F}(\omega, t) = \int_0^t d\tau \int_0^t d\tau' e^{-i\omega(\tau - \tau')} \hat{R}_Z^T(\tau) \hat{R}_Z(\tau') \qquad (10)$$

depends on fast rotations around the local spin quantization axis $[R_3(\Phi_B)]$, which account for the phase accumulated because of the Zeeman energy $|\boldsymbol{\omega}_B|/2\pi \sim 10$ GHz, and on slower rotations of about 10–100 MHz of the spin quantization axis $[R_B(\theta_B)]$ caused by the motion of the spin in an inhomogeneous Zeeman field.

In realistic semiconducting devices, the spectral function $S(\omega)$ is strongly peaked at low frequencies and has a $1/\omega$ tail at large frequencies [18,113,114]. Because the transversal elements of $\hat{F}$ contain rapidly oscillating terms determined by Φ_B, they are peaked at large frequencies in

the gigahertz range, where the noise has less weight. For this reason, the dominant contribution to the fidelity arises from the longitudinal element of the covariance matrix $\hat{\Sigma}_{33}$, which is peaked at low frequencies, and is determined by the element $\hat{F}_{33} \equiv F$,

$$F(\omega, t) = \int_0^t d\tau \int_0^t d\tau' e^{-i\omega(\tau-\tau')} \frac{\boldsymbol{\omega}_B[\bar{z}(\tau)]}{|\boldsymbol{\omega}_B[\bar{z}(\tau)]|} \cdot \frac{\boldsymbol{\omega}_B[\bar{z}(\tau')]}{|\boldsymbol{\omega}_B[\bar{z}(\tau')]|}, \tag{11}$$

of the matrix of filter functions $\hat{F}$ [115]. In this case, the average shuttling fidelity becomes

$$\bar{\mathcal{F}} = e^{-\hat{\Sigma}_{33}/8}. \tag{12}$$

We note that the corrections coming from the fast-rotating transversal terms causing spin relaxation lead to a power-law decay, with slower time constants, instead of the faster exponential decay included here [86,89,111,112].

Equations (11) and (12) highlight the fundamental role that the inhomogeneity of the Zeeman field has in determining the average shuttling fidelity $\bar{\mathcal{F}}$. In particular, the inhomogeneous tilt of the spin quantization axis encoded in the product $\boldsymbol{\omega}_B[\bar{z}(\tau)] \cdot \boldsymbol{\omega}_B[\bar{z}(\tau')]$ can substantially impact the filter function. We discuss this phenomenon in the next section by analyzing a few key examples. A comparison between the filter functions and average shuttling fidelities obtained for different cases is shown in Fig. 2.

C. Suppressing noise by shuttling

1. Spin rotation in homogeneous Zeeman fields

We consider first the simplest case where during shuttling the spin moves in a homogeneous Zeeman field, i.e., $\tilde{\boldsymbol{\omega}}_B(z) = \boldsymbol{\omega}_B(z) = \omega_B \mathbf{n}_3$. This case is the aim of most current experimental settings in silicon [73], but we show that it does not always correspond to the highest shuttling fidelity, especially in material such as germanium, where the inhomogeneities of the Zeeman field are intrinsically large [70].

If the Zeeman field does not depend on space, the unitary time-evolution operator of the spin given in Eq. (3) reduces to the simple phase accumulation $U_Z = e^{-i\omega_B t\sigma_3/2}$, which rotates the spin around the fixed axis $\mathbf{n}_3$. Moreover, the product $\boldsymbol{\omega}_B[\bar{z}(\tau)] \cdot \boldsymbol{\omega}_B[\bar{z}(\tau')] = 1$ and the longitudinal filter function F in Eq. (11) simplifies to

$$F(\omega, t) = \frac{4 \sin^2(\omega t/2)}{\omega^2} \equiv F_{\text{FID}}(\omega, t), \tag{13}$$

which corresponds to the filter function of a free-induction decay (FID) experiment [96].

We remark that F_{FID} is peaked at zero frequency $\omega = 0$, where it grows as $F_{\text{FID}}(\omega = 0, t) = t^2$; see the black line in
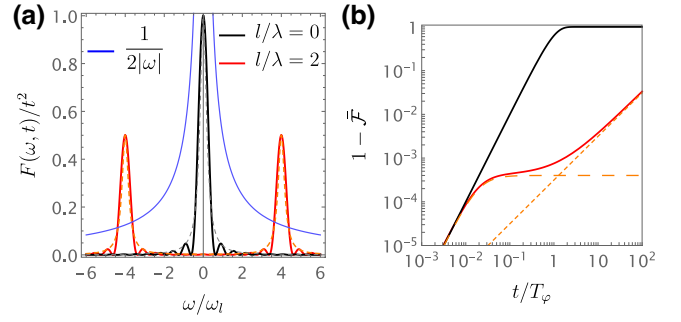

FIG. 2. Enhancing the shuttling fidelity by an inhomogeneous Zeeman field. We consider here global noise sources and the Zeeman field in Eq. (17). (a) Filter functions. With a black and red curve, we show the filter functions of a shuttling experiment in a homogeneous and an inhomogeneous Zeeman field rotating with period $\lambda = l/2$ [see Eq. (17)], respectively. The solid lines show the exact filter functions given in Eqs. (13) and (D1a), while the dashed lines show the approximated result in Eq. (19). For reference, we show with a blue line a typical spectral function of the noise $S(\omega) \propto |\omega|^{-1}$. We consider ω in units of $\omega_l = \bar{v}/l$ and we used $t = 10/\omega_l$. (b) Shuttling fidelity. Comparison of the infidelity $1 - \bar{\mathcal{F}}$ in a doubly logarithmic plot. The time is measured in units of the dephasing time T_φ. A finite λ improves the shuttling fidelity for global noise sources, as one can observe by comparing the black ($\lambda \to \infty$) and red ($\lambda = l/2$) curves. Solid lines show the exact results in Eqs. (15) and (D1b) and dashed lines show the limiting cases in Eq. (20). We consider a noise with $\eta = 0.01$ and $\omega_\lambda = \bar{v}/\lambda = 50/T_\varphi$, corresponding to $\omega_\lambda/2\pi \approx 8$ MHz for typical values $T_\varphi \approx 1 \, \mu$ s.

Fig. 2(a). For this reason, the shuttling fidelity $\bar{\mathcal{F}}$, related to the longitudinal component $\hat{\Sigma}_{33}$ of the covariance matrix by Eq. (12), is determined by low-frequency noise that dominates the integral in Eq. (9).

To explicitly compare different scenarios, we use here the typical spectral function measured in experiments [18, 113]

$$S(\omega) = \frac{2\pi \hbar^2}{T^{2-\eta}} \frac{1}{|\omega|^{1-\eta}}, \tag{14}$$

where $\eta \in (0, 1]$ and we have introduced the time scale $T > 0$ that characterizes the amplitude of the noise fluctuations in different experiments. While $S(\omega)$ in Eq. (14) describes charge noise, we stress that our results are general and applicable to all types of low-frequency noise, notably including the hyperfine noise caused by spinful nuclear defects. In particular, combining Eqs. (9), (12), and (13), we find that, for the FID, the average shuttling fidelity is

$$\bar{\mathcal{F}}_{\text{FID}} = e^{-(t/T)^{2-\eta} \cos(\pi\eta/2)\Gamma(\eta-2)/2} \approx e^{-t^2/T_\varphi^2},$$
$$T_\varphi = 2T\sqrt{\eta}, \tag{15}$$

where $\Gamma(x)$ is the gamma function. The approximation reports the purely pink noise case, with $\eta \to 0^+$, such

that the noise spectrum is $S(\omega) \propto 1/|\omega|$; see the blue line in Fig. 2(a). Importantly, we stress that the dephasing time $T_\varphi \propto \sqrt{\eta}$ vanishes for purely $1/|\omega|$ noise because of the characteristic nonintegrable divergence at zero frequency. We point out that an alternative way to regularize this infrared divergence requires a cut-off frequency ω_{ir}, that could be physically related to the running time of the experiment and introduces the typical logarithmic correction $T_\varphi \propto \sqrt{1/\log(\omega_{\text{ir}}t)} \to 0$ as $\omega_{\text{ir}} \to 0^+$ [116].

The average shuttling infidelity $1 - \bar{\mathcal{F}}$ for FID is shown with a black line in Fig. 2(b), and it will serve as a reference to compare different cases. For typical experimental values of $T_\varphi \sim 1\,\mu s$ [6,18,90,113] and shuttling velocities of about 1 m/s, we obtain a loss of coherence of the spin within a distance $\bar{z} \sim 1\,\mu m$. Finally, we remark here that, as long as the motion of the spin remains adiabatic compared to orbital and Zeeman fields, the shuttling fidelity of FID is independent of the velocity of the quantum dot. This is not generally valid in the presence of inhomogeneity of the Zeeman field, as we discuss next.

2. Spin precession in inhomogeneous Zeeman fields

In striking contrast to the FID case, if the Zeeman field is inhomogeneous, the time dependence of the product $\boldsymbol{\omega}_B[\bar{z}(\tau)] \cdot \boldsymbol{\omega}_B[\bar{z}(\tau')]$ in Eq. (11) shifts the weight of the longitudinal filter function F to frequencies of tens of megahertz, thus significantly improving the average shuttling fidelity.

To illustrate this effect, we first consider a simple scenario where the moving spin precesses in the inhomogeneous Zeeman field

$$\frac{\tilde{\boldsymbol{\omega}}_B^{\text{P}}(z)}{\tilde{\omega}_B} = \cos\left(\frac{2z}{\lambda}\right)\mathbf{n}_3 + \sin\left(\frac{2z}{\lambda}\right)\mathbf{n}_2 = \hat{R}_1\left(\frac{2z}{\lambda}\right)\mathbf{n}_3 \quad (16)$$

that fully rotates around a fixed axis. Matrix $\hat{R}_1$ is reported in Appendix B and describes a rotation around $\mathbf{n}_1 = (1, 0, 0)$ with period $\pi\lambda$.

While being an ideal field, we emphasize that $\boldsymbol{\omega}_B^{\text{P}}$ nicely describes a wide variety of devices. For example, in electronic systems $\boldsymbol{\omega}_B^{\text{P}}$ matches the stray magnetic field produced by modular nanomagnets spaced by a distance $\pi\lambda$ [99]. In this case, we note that a small homogeneous magnetic field is required to polarize the magnets, but this field could be switched off after the initial polarization. Moreover, in planar hole nanostructures, $\tilde{\boldsymbol{\omega}}_B^{\text{P}}$ reasonably approximates the strain and electric-field-induced tilting of the g tensor [84,85] caused by the periodic arrangement of gates required for a conveyer-mode shuttling architecture. For example, in neighboring quantum dots defined in planar germanium heterostructures, g tensors tilting by more than 40% [70], and even g factors with opposite signs [107], have been recorded, suggesting that fully rotating fields as $\tilde{\boldsymbol{\omega}}_B^{\text{P}}$ could be engineered in these systems.

A detailed discussion of the effects of residual homogeneous Zeeman fields is delayed to Sec. III C 3 below. We also emphasize that, while we focus on fully rotating Zeeman fields in this section, our protocol to improve shuttling fidelity can be adapted to weakly inhomogeneous fields, as discussed in detail in Sec. V B below. We anticipate that the field $\tilde{\boldsymbol{\omega}}_B^{\text{P}}$ matches the effective Zeeman field produced by a finite SOI, as typical in hole nanowires and fin field-effect transistors, as we show in Sec. IV below. We also remark that in this section we consider noise that is not modulated by the inhomogeneity of the Zeeman field; because such modulated noise naturally emerges when including an SOI, we postpone the discussion to Sec. IV.

The Zeeman energy of the moving quantum dot appearing in H_Z in Eq. (2) is

$$\boldsymbol{\omega}_B^{\text{P}}(\bar{z}) = \omega_B \hat{R}_1\left(\frac{2\bar{z}}{\lambda}\right)\mathbf{n}_3 \quad \text{with} \quad \omega_B = e^{-l^2/\lambda^2}\tilde{\omega}_B, \quad (17)$$

and is related to the local Zeeman energy $\tilde{\boldsymbol{\omega}}_B^{\text{P}}(z)$ in H_{1D} in Eq. (1) by the well-known Gaussian renormalization factor e^{-l^2/λ^2}, which accounts for the effects of strong confinement and large inhomogeneity in the z direction [78,81–83].

In this case, the time-evolution operator in Eq. (3) and the kernel of the longitudinal filter function F in Eq. (11) respectively reduce to

$$U_Z^{\text{P}}(t) = e^{-i\bar{z}(t)\sigma_1/\lambda}e^{-i\omega_B t\sigma_3/2},$$
$$\frac{\boldsymbol{\omega}_B[\bar{z}(\tau)]}{|\boldsymbol{\omega}_B[\bar{z}(\tau)]|} \cdot \frac{\boldsymbol{\omega}_B[\bar{z}(\tau')]}{|\boldsymbol{\omega}_B[\bar{z}(\tau')]|} = \cos\left[2\frac{\bar{z}(\tau) - \bar{z}(\tau')}{\lambda}\right]. \quad (18)$$

In contrast to FID, in an inhomogeneous Zeeman field the quantum dot motion plays a critical role because the energetically favored spin quantization axis varies at different positions and times. This results in spin precession during shuttling.

Considering a constant shuttling velocity $\bar{z}(t) = \bar{v}t$, the integral in Eq. (11) defining F can be evaluated exactly, and the complete solution is provided in Appendix D; see Eq. (D1b). We find that an accurate approximation for the exact result is provided by the simple equation

$$F_{\text{P}}(\omega, t) \approx \frac{t^2}{2}\left[f_L\left(\frac{\omega - 2\omega_\lambda}{2/t}\right) + f_L\left(\frac{\omega + 2\omega_\lambda}{2/t}\right)\right], \quad (19)$$

where $f_L(x) = (1 + x^2)^{-1}$ is a Lorentzian function normalized as $f_L(0) = 1$. We introduce here the relevant frequency shift $\omega_\lambda = \bar{v}/\lambda$, quantifying the rate of change in the spin quantization axis; in a similar way, we also define the frequency $\omega_l = \bar{v}/l$.

In Fig. 2(a), we show a comparison between the exact (solid lines) and approximate (dashed lines) solutions. Importantly, F_{P} comprised two functions peaked at finite

frequencies $\pm 2\omega_\lambda$ and with broadening $1/t$ becoming narrower at large times. By considering state-of-the-art experiments, we assume an adiabatic shuttling velocity $\bar{v} = 1$ m/s, commonly achieved in conveyer-mode shuttling experiments [71], and a gate pitch of $\pi\lambda = 50$ nm, typical in germanium [6,70] and consistent with recent experiments with nanomagnets [99]. For these realistic parameters, we find that $\omega_\lambda/2\pi = 10$ MHz, which substantially shifts the relevant components of noise toward megahertz frequencies, where the noise has lower weight (blue line). This shift is equivalent to an intrinsic dynamical decoupling of the largest low-frequency noise.

Considering pink noise with the spectral function $S(\omega)$ in Eq. (14), and using Eqs. (9), (12), and (19), we can estimate the shuttling fidelity. The complete equation is provided in Eq. (D1a) in Appendix D and is shown with a solid red line in Fig. 2(b). For pure $1/|\omega|$ noise ($\eta \to 0^+$), this function can be approximated by

$$\bar{\mathcal{F}}_P \approx \begin{cases} e^{-t^2/T_\varphi^2}, & t \lesssim 1/\omega_\lambda, \\ e^{-\omega_\lambda^2 T_\varphi^2}, & 1/\omega_\lambda \lesssim t \lesssim T_P = 8\omega_\lambda T^2/\pi, \\ e^{-t/T_P}, & t \gtrsim T_P, \end{cases} \quad (20)$$

and nicely matches the limiting behavior of $\bar{\mathcal{F}}_P$; see the dashed lines in Fig. 2(b). Here, T_φ is the FID dephasing time given in Eq. (15). At small values of $\omega_\lambda t$, corresponding to a few spin rotations during shuttling, $\bar{\mathcal{F}}_P \approx \mathcal{F}_{FID}$. However, if the spin experiences many rotations during shuttling and $\omega_\lambda T_\varphi \gtrsim 1$, the fidelity first saturates to a finite value following the interpolation function $\bar{\mathcal{F}}_P \approx e^{-t^2 f_L(\omega_\lambda t)/T_\varphi^2}$, and then decays exponentially with a longer time constant T_P that is *independent* of the small diverging cutoff $\eta \to 0^+$.

Considering the realistic value $\omega_\lambda/2\pi \approx 10$ MHz estimated for state-of-the-art experiments and $T_\varphi = 1$ μs, typical for current spin qubits [6,90], we find a significant improvement in the shuttling fidelity by the inhomogeneous magnetic field compared to the FID, as shown in Fig. 2(b), with infidelities that remain below 10^{-3} for a much wider range of shuttling times. Because of the intrinsic dynamical decoupling of low-frequency noise, the inhomogeneous Zeeman field boosts the possible shuttling times to times a few orders of magnitude larger than the dephasing time T_φ, corresponding to a coherent shuttling over distances larger than 100 μm.

We also note that while we assumed for simplicity a constant absolute value of the Zeeman frequency ω_B [see Eq. (17)], because the term dominating the fidelity is independent of ω_B, our results also remain approximately valid when ω_B has a spatial dependence, e.g., an additional oscillatory component with period $\pi\lambda$, provided that the minimal Zeeman frequency ω_B^{min} remains large compared to ω_λ. More details on the effects of inhomogeneous $\omega_B(\bar{z})$ are provided in Sec. V below.

3. Spin nutation in inhomogeneous Zeeman fields

We now show that the enhancement of fidelity by an inhomogeneous Zeeman field occurs in more general cases. In particular, here we study the nutating dynamics of a moving spin in the Zeeman field

$$\boldsymbol{\omega}_B^N(\bar{z}) = \omega_B \hat{R}_N\left(\frac{2\bar{z}}{\lambda}\right)\mathbf{n}_3 \quad (21)$$

that rotates around an inhomogeneous vector. Matrix $\hat{R}_N$ describes a general rotation around the oscillating unit vector

$$\mathbf{n}_N(z) = \frac{\mathbf{n}_1}{\sqrt{1+A^2}} + \frac{A[\cos(2\bar{z}/\lambda_N)\mathbf{n}_3 - \sin(2\bar{z}/\lambda_N)\mathbf{n}_2]}{\sqrt{1+A^2}}. \quad (22)$$

We refer to this process as a nutation out of phase because the rotation of $\mathbf{n}_N$ is out of phase compared to the precessing Zeeman field; see Eq. (16). The amplitude of the nutation is characterized by the dimensionless constant A and by its period λ_N, which does not need to match the period λ of the precession. We also only consider the cases where $\omega_\lambda \sim \omega_N \ll \omega_B$, with $\omega_N = \bar{v}/\lambda_N$.

Using Eq. (B3) in Appendix B, we can easily evaluate $\boldsymbol{\omega}_B^N(\bar{z})$. The components of the out-of-phase nutating Zeeman field are shown with solid lines in Fig. 3(a). Compared to the rotating Zeeman field $\boldsymbol{\omega}_B^P$ in Eq. (17), $\boldsymbol{\omega}_B^N$ includes an additional component oscillating in the x direction (red line). This oscillating term produces on average the finite homogeneous Zeeman field $-\omega_B A/(1+A^2)$, and thus $\boldsymbol{\omega}_B^N$ nicely describes the effects of residual homogeneous fields in realistic experiments. These fields can occur because of nonzero polarizing magnetic field for electronic systems with nanomagnets [99] or nonfully precessing g tensors in hole nanostructures [70]. Here, we restrict ourselves to the case $A \ll 1$ and we show that in this case the shuttling fidelity is still strongly enhanced; however, we anticipate that similarly high fidelities can also be engineered by increasing $\bar{v}$ when the residual homogeneous field is large, as we discuss in detail in Sec. V below.

The spin dynamics in this case is well approximated by the time-evolution operator

$$U_Z^N(t) = e^{-i\bar{z}(t)\mathbf{n}_N[2\bar{z}(t)/\lambda_N]\cdot\boldsymbol{\sigma}/\lambda} e^{-i\omega_B t\sigma_3/2}, \quad (23)$$

describing a spin nutation. The longitudinal filter function F in Eq. (11) can be evaluated numerically. In the limit of small A, we find that $F_N = F_P - \delta F_N$, with

$$\delta F_N \approx \frac{A^2 t^2}{4}\left[2f_L\left(\frac{\omega - 2\omega_\lambda}{2/t}\right) - f_L\left(\frac{\omega - 2\omega_N}{2/t}\right) - f_L\left(\frac{\omega - 2\omega_\lambda + 2\omega_N}{2/t}\right)\right] + (\omega \to -\omega). \quad (24)$$
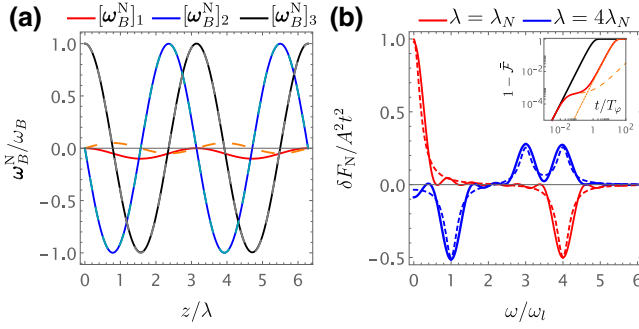
FIG. 3. Nutating Zeeman field. (a) Spatial dependence of the inhomogeneous field. We show with red, blue, and black the three components of the field $\boldsymbol{\omega}_B^N$. Solid (dashed) lines represent the out-of-phase (in-phase) nutation given by Eqs. (21) and (22) [Eqs. (21) and (26)]. The only component that is significantly modified in the two cases is the Zeeman field in the x direction (red). Here we use $A = 0.05$ and $\lambda_N = \lambda$. (b) Correction to the longitudinal filter function δF caused by out-of-phase nutation. Red (blue) lines show the resonant (off-resonant) case with $\lambda = \lambda_N = l/2$ ($\lambda = 4\lambda_N = l/2$). Solid lines show the exact solution for δF_N, while the dashed lines show the approximation in Eq. (24). Here we use $t = 10/\omega_l$. In the double logarithmic plot in the inset, we show with a red solid line the infidelity of shuttling in an out-of-phase resonant nutating Zeeman field; see Eq. (25). The black and dashed orange lines show for reference the infidelity for a FID and a precessing field; see Fig. 2(b). The dotted orange line represents the contribution of the additional dephasing time T_φ^N. Here, $A = 0.05$, $\lambda = \lambda_N = l/2$, and $\omega_\lambda = 50/T_\varphi$.

Here, the notation $\omega \rightarrow -\omega$ indicates that in the brackets there are three additional Lorentzian peaks obtained from those reported by inverting the frequency, and we neglected corrections $\mathcal{O}(A^4)$ and combing from oscillations at higher frequencies.

The corrections δF_N to the precessing filter function F_P coming from out-of-phase nutation are shown with red and blue lines in Fig. 3(b) for different values of λ/λ_N. We observe good agreement between the approximated equation (24) (dashed lines) and the exact solution (solid lines). Importantly, nutation introduces sideband peaks at frequencies $\omega = \pm 2\omega_N$ and $\omega = \pm 2(\omega_\lambda - \omega_N)$ with amplitude $\propto A^2$. When the period of nutation λ_N is much shorter than the period of precession λ, and $\lambda_N \lesssim \lambda/2$, these sideband peaks sample noise at high frequency, yielding negligible corrections to F_P (blue lines). In contrast, when $\lambda_N \gtrsim \lambda/2$, the sideband peaks of δF_N occur at low frequencies. This effect results in a resonant condition at $\lambda_N = \lambda$, where the side peaks merge into the Lorentzian peak $A^2 t^2 f_L(\omega t/2)$ sampling the noise at $\omega = 0$ (red lines).

In this resonant scenario, and for the $1/|\omega|$ noise given in Eq. (14), the average shuttling fidelity acquires a significant correction and becomes

$$\mathcal{F}_N \approx \mathcal{F}_P e^{-t^2/T_N^2} \quad \text{with} \quad T_N = T_\varphi/A. \tag{25}$$

This fidelity is shown in the inset of Fig. 3(b). Compared to the dephasing time T_φ in Eq. (15), the time constant of the Gaussian decay is enhanced by the small amplitude of the nutation A. This decay time dominates the fidelity in the long time asymptotic.

The dependence of T_N on A can be understood in general by considering that at $\lambda = \lambda_N$ the out-of-phase nutating Zeeman field in Eq. (21) contains on average the homogeneous component $-A\mathbf{n}_1/(1 + A^2) \approx -A^2\mathbf{n}_1$ along the main precession axis. This residual homogeneous field causes a constant dephasing during shuttling with time constant $T_\varphi(1 + A^2)/A = T_N + \mathcal{O}(A^2)$. This interpretation clearly shows that, when the spin degree of freedom is moved adiabatically compared to the Zeeman energy, the maximal enhancement of coherence occurs for effective inhomogeneous Zeeman fields that fully rotate during shuttling.

We emphasize that the worst-case scenario presented here, where $\lambda = \lambda_N$, also requires the nutation in Eq. (21) to be out of phase. When the nutation is in phase and is generated, for example, by the vector

$$\mathbf{n}_N(z) = \frac{\mathbf{n}_1}{\sqrt{1 + A^2}} + \frac{A[\cos(2\bar{z}/\lambda_N)\mathbf{n}_3 + \sin(2\bar{z}/\lambda_N)\mathbf{n}_2]}{\sqrt{1 + A^2}}, \tag{26}$$

there is on average no homogeneous Zeeman field along the main precession axis [see the dashed lines in Fig. 3(a)], and thus $T_N \rightarrow \infty$.

D. Local noise sources

The noise model introduced in Eq. (4) assumes that during the shuttling the spin experiences a random time-dependent Zeeman field $\mathbf{h}(t)$ that is homogeneous in space. This model describes global noise sources originating, for example, from the fluctuation of the externally applied magnetic field or long-range electric fields. Here, we analyze the effect of an inhomogeneous noise distribution during shuttling. We focus, in particular, on an ensemble of short-range impurities at fixed positions $z = z_k$ that couple to the spin via local interactions $\mathbf{h}_k(t)$. This model describes well nuclear spins and local dynamical charge traps electrostatically coupled to the dot.

In this case, the local noise Hamiltonian is

$$H_N = \frac{1}{2n_0} \sum_k \delta(z - z_k)\mathbf{h}_k(t) \cdot \boldsymbol{\sigma}, \tag{27}$$

where n_0 is the atomic density and $\delta(z)$ is the delta function. The spin confined in the moving quantum dot has a charge density $|\psi[z - \bar{z}(t)]|^2 \approx e^{-[z-\bar{z}(t)]^2/l^2}/l\sqrt{\pi}$ and

experiences the time-dependent noise

$$H_N^L = \frac{1}{2n_0} \sum_k |\psi[z_k - \bar{z}(t)]|^2 \mathbf{h}_k(t) \cdot \boldsymbol{\sigma}. \quad (28)$$

Proceeding as in Sec. III B, assuming an isotropic and spatially uncorrelated noise with $\langle \mathbf{h}_k^n(t)\mathbf{h}_{k'}^m(0)\rangle = \delta_{kk'}\delta_{nm}\int d\omega e^{-i\omega t}S(\omega)/2\pi$, and using the envelope function approximation $\sum_k \to \nu n_0 \int dz$, where ν is the average percentage of defects, we find that, for local noise sources, the longitudinal component of the filter function modifies as

$$F^L(\omega, t) = \frac{\nu}{N}\int_0^t d\tau \int_0^t d\tau' e^{-i\omega(\tau-\tau')}e^{-[\bar{z}(\tau)-\bar{z}(\tau')]^2/2l^2}$$
$$\times \frac{\boldsymbol{\omega}_B[\bar{z}(\tau)]}{|\boldsymbol{\omega}_B[\bar{z}(\tau)]|} \cdot \frac{\boldsymbol{\omega}_B[\bar{z}(\tau')]}{|\boldsymbol{\omega}_B[\bar{z}(\tau')]|}, \quad (29)$$

where $N = \sqrt{2\pi}ln_0$ is the number of atoms in the dot. More detailed derivations of F^L, also including more general noise sources, are provided in Appendix C. Importantly, for local noise sources, the kernel of the filter function includes the additional weight $e^{-[\bar{z}(\tau)-\bar{z}(\tau')]^2/2l^2}$ that accounts for the locality of the noise and the spatial distribution of the spin. This term describes the motional narrowing of inhomogeneous noise during shuttling [73].

To illustrate its effect explicitly, here we consider the precessing Zeeman field $\boldsymbol{\omega}_B^P$ given in Eq. (17). The coherent dynamics of the spin is not altered and the spin precesses according to the time-evolution operator U_Z^P in Eq. (18). However, the longitudinal filter function F_P^L is significantly modified. By combing Eqs. (17) and (29), we derive an exact solution, reported in Eq. (D1b) in Appendix D. In analogy to the global noise solution F_P in Eq. (19), we find that F_P^L can be approximated by

$$F_P^L \approx \frac{\nu}{N}\frac{t}{2\omega_l}\left[f_G\left(\frac{\omega - 2\omega_\lambda}{\omega_l}\right) + f_G\left(\frac{\omega + 2\omega_\lambda}{\omega_l}\right)\right] \quad (30)$$

with $f_G(x) = e^{-x^2/2}$ a Gaussian normalized to $f_G(0) = 1$. As shown in Fig. 4(a), we observe a good match between the exact and approximated solutions (solid and dashed lines, respectively).

While qualitatively F_P^L and F_P show similar behavior with the peaks of the filter function being shifted by the finite λ to the higher frequencies $\pm 2\omega_\lambda$, with $\omega_\lambda = \bar{v}/\lambda$, we emphasize that there are a number of key differences between the two cases; see Eqs. (19) and (30). First, for local noise, the peaks of F_P^L have a Gaussian lineshape that originates from the approximated charge density of the quantum dot $|\psi(z)|^2$ in contrast to the Lorentzian peaks of F_P. Moreover, the broadening of the Gaussian peaks of F_P^L is time independent and it is determined by the characteristic frequency $\omega_l = \bar{v}/l$. Finally, we observe that $F_P^L \propto t/\omega_l$,
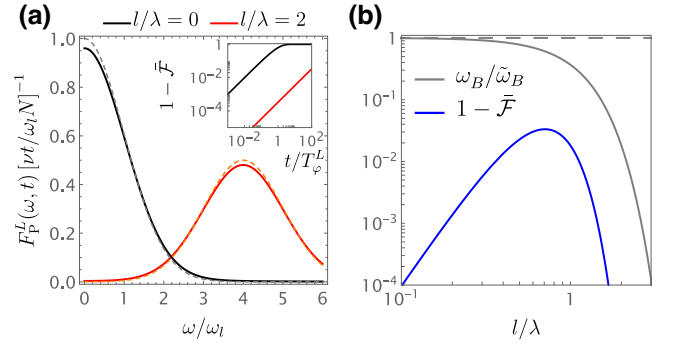

FIG. 4. Local noise sources. (a) Filter function and average shuttling fidelity for spin precessing in an inhomogeneous Zeeman field. Red and black curves represent the filter functions F_P^L obtained at $l/\lambda = 0$ and $l/\lambda = 2$, respectively. Solid (dashed) lines show the exact (approximate) solution in Eq. (D1b) [Eq. (30)]. Here we used $t = 20/\omega_l$. In the inset, we show with a double logarithmic plot their corresponding average shuttling infidelity as a function of time; see Eq. (31). (b) Dependence of the shuttling infidelity and of the Zeeman energy on the inhomogeneity of the Zeeman field. In this double logarithmic plot, the blue curve represents the average shuttling as a function of l/λ at the fixed time $t = T_0$ obtained by combining Eqs. (31) and (34). With gray lines, we show the corresponding Zeeman energy ω_B^P. The solid line represents the Zeeman energy $\boldsymbol{\omega}_B^P$ in Eq. (17), which is renormalized by e^{-l^2/λ^2} and obtained for a dot moving adiabatically compared to the Zeeman field, while the dashed line represents the Zeeman energy $\boldsymbol{\omega}_B^D$ in Eq. (63) when this adiabaticity condition is lifted.

while for global noise, $F_P \propto t^2$, thus strongly impacting the average shuttling fidelity $\bar{\mathcal{F}}$.

By considering the charge noise spectrum $S(\omega)$ in Eq. (14), we find that, for local noise sources,

$$\bar{\mathcal{F}}_P^L = \exp\left\{-2^{(\eta-6)/2}\frac{\nu t}{NT}\Gamma\left(\frac{\eta}{2}\right)(\omega_l T)^{\eta-1}\right.$$
$$\left. \times {}_1F_1\left(\frac{1-\eta}{2}; \frac{1}{2}; \frac{-2l^2}{\lambda^2}\right)\right\} \approx e^{-t/T_\varphi^L}, \quad (31)$$

$$T_\varphi^L = \omega_l\left(\sqrt{\frac{N}{\nu}}T_\varphi\right)^2 e^{2l^2/\lambda^2},$$

where ${}_1F_1(a; b; c)$ is the hypergeometric function. We note that, when the quantum dot is static, the FID dephasing times due to global and local noise are $T_\varphi = 2T_\varphi\sqrt{\eta}$ [see Eq. (15)] and $\sqrt{N/\nu}T_\varphi$, respectively, where the factor $\sqrt{N/\nu}$ accounts for the average percentage of local defects in the quantum dot [89,111,112].

In the inset of Fig. 4(a), we show the average shuttling infidelity for local noise sources, comparing the homogeneous $\lambda \to \infty$ (black curve) and precessing $\lambda = l/2$ (red curve) Zeeman field cases. In contrast to $\bar{\mathcal{F}}_P$ in Eq. (20), the shuttling fidelity $\bar{\mathcal{F}}_P^L$ follows an exponential decay with the time constant T_φ^L being significantly larger than for

the global noise case because of the motional narrowing of local fluctuators. This effect can be clearly observed by considering homogeneous Zeeman fields, and observing that, for typical values of $\omega_l \sim 10$–100 MHz and $\sqrt{N/\nu}T_\varphi \sim 0.1$–$10$ μs, $T_\varphi^L \gtrsim 10\sqrt{N/\nu}T_\varphi$ also at $\lambda \to \infty$.

The additional spin dynamics in the inhomogeneous field produces an additional beneficial effect that is encoded in the Gaussian correction e^{2l^2/λ^2} in Eq. (31). As a consequence, low-frequency local noise is substantially filtered out by the inhomogeneous field in long quantum dots with $l \gtrsim \lambda$; see Fig. 4(a). However, we note that in long quantum dots the effective Zeeman energy ω_B is also reduced by a weaker Gaussian correction e^{-l^2/λ^2} [see Eq. (17)], thus limiting the maximal values of the useful l/λ ratio. This trade-off is highlighted in Fig. 4(b) by comparing solid blue and gray lines that represent T_φ^L and ω_B, respectively. Considering, for example, a typical gate pitch of $\pi\lambda \approx 50$ nm and realistic values of the quantum dot length, $l \approx 20$ nm, we observe a significant reduction of the noise with $T_\varphi^L \approx 20 T_\varphi^L(l/\lambda = 0)$, still preserving a large Zeeman gap $\omega_B \approx 0.2\tilde{\omega}_B$ at realistic values of the magnetic field of about 1 T. We anticipate that this trade-off between fidelity and Zeeman energy can be lifted by higher shuttling velocities that are not adiabatic with respect to the Zeeman energy [see the dashed gray curve], as we discuss in Sec. V below.

For completeness, here we explicitly show that the enhancement of the shuttling fidelity also appears when one considers the hyperfine noise caused by an ensemble of spinful nuclear defects. In the experimentally relevant case, where nuclear spins are sparse and have a slow dynamics, their noise spectral function is peaked at low frequency and is well approximated by $S_{\mathrm{HF}}(\omega) = 2\pi\hbar^2\delta(\omega)/T^2$, with a characteristic time T dependent on several microscopic details of the system [89,111]. In agreement with Eq. (31), by combining Eqs. (9), (12), and (30) with spectral function $S_{\mathrm{HF}}(\omega)$, we find an exponential decay of the fidelity with timescale $T_{\mathrm{HF}} = \omega_l(T_\varphi^{\mathrm{HF}})^2 e^{2l^2/\lambda^2}$ and a hyperfine-noise-induced FID time $T_\varphi^{\mathrm{HF}} = 2\sqrt{2N/\nu}T \sim 1$ μs in natural silicon and germanium [89,117].

E. Charge noise in inhomogeneous Zeeman fields

We showed that an inhomogeneous Zeeman field dynamically decouples the moving spin from the dominant low-frequency noise, and thus provides an effective way to filter out the noise caused, for example, by hyperfine interactions with nuclear spins. However, more care is required to analyze its effect on charge noise, because Zeeman field inhomogeneities characterized by the ratio l/λ also render the spin susceptible to the fluctuations of the electrostatic environment, thus directly coupling the spin to these charge noise sources. For this reason, current shuttling experiments minimize the inhomogeneity of the field and

operate at $l/\lambda \ll 1$. We show here that while this approach indeed provides a coherent shuttling, the inhomogeneity-induced intrinsic dynamical decoupling also enables large shuttling fidelities at $l/\lambda \gtrsim 1$. In particular, the time scale T characterizing the noise spectral function $S(\omega)$ in Eq. (14) also depends on l/λ, thus further influencing the time T_φ.

To quantify this effect, we focus on the precessing spins discussed in Sec. III C 2 and we explicitly include the coupling of the spin to charge noise due to the Gaussian renormalization of the Zeeman energy $\omega_B = e^{-l^2/\lambda^2}\tilde{\omega}_B$ given in Eq. (17). Focusing on a local noise source labeled by k, small random variations $\delta V_k(t)$ of the electrostatic environment cause fluctuations of length l and couple directly to the Zeeman energy, resulting in the noise field [88]

$$\mathbf{h}_k(t) \approx \hbar\boldsymbol{\omega}_B^{\mathrm{P}}(z_k)\left[\frac{\partial_V\tilde{\omega}_B}{\tilde{\omega}_B} - \frac{2l^2}{\lambda^2}\frac{\partial_V l}{l}\right]\delta V_k(t). \quad (32)$$

Here, we introduced the susceptibilities $\partial_V l$ and $\partial_V\tilde{\omega}_B$ of length l and of the local Zeeman field $\tilde{\omega}_B$ to variations in the environment. Moreover, we assumed that charge defects have a local effect on the spin [see Eq. (28)]; however, we point out that a similar noise Hamiltonian can be derived for global noise sources; corrections coming from intermediate-range noise are discussed in Appendix C.

Now introducing the pure $1/f$ charge noise spectral density $S_{\delta V}(\omega) = \bar{V}^2/|\omega|$, such that $\langle \delta V_k(t)\delta V_{k'}(0)\rangle = \delta_{kk'}\int d\omega S_{\delta V}(\omega)/2\pi$, we find the functional dependence of the time scale T in Eq. (14) to be

$$T = \frac{\sqrt{2\pi}}{\bar{V}\tilde{\omega}_B e^{-l^2/\lambda^2}}\left|\frac{\partial_V\tilde{\omega}_B}{\tilde{\omega}_B} - \frac{2l^2}{\lambda^2}\frac{\partial_V l}{l}\right|^{-1}. \quad (33)$$

Away from sweet spots where $T \to \infty$ [88] and by combining Eqs. (31) and (33) we find that

$$T_\varphi^L \approx T_0\frac{\lambda^4}{l^4}e^{4l^2/\lambda^2} \quad \text{with} \quad T_0 = 2\pi\eta\frac{N}{\nu}\frac{\omega_l}{\tilde{\omega}_B^2}\frac{l^2}{\bar{V}^2(\partial_V l)^2}. \quad (34)$$

Here we discarded the term $\propto \partial_V\tilde{\omega}_B$ that is independent of l/λ and is therefore clearly filtered out by the inhomogeneous field.

The functional dependence of the average shuttling fidelity on the inhomogeneity of the Zeeman field is illustrated in Fig. 4(b) with a blue curve. As expected, for small values of l/λ when the Zeeman field is rather homogeneous, the time constant T_φ^L determining the shuttling fidelity decreases as $\propto l^4/\lambda^4$, resulting in an lower shuttling fidelity. This power law is related to the typical scaling of the FID dephasing time $T_\varphi \propto l^2/\lambda^2 \propto \sqrt{T_\varphi^L}$ [88]; we also note that relaxation processes scale as the square of the inhomogeneity [118]. In this regime, the noise is dominated by the variations $\propto \partial_V\tilde{\omega}_B$ or by nuclear spin noise

that is independent of λ. However, if the Zeeman field inhomogeneity is large and $l/\lambda \gtrsim 1$, the induced intrinsic dynamical decoupling of the spin becomes effective and rapidly increases the shuttling fidelity. This same trend also occurs as a function of the SOI, as we show in the following section.

IV. SPIN-ORBIT INTERACTION

The SOI causes a spin rotation depending on the velocity of the particle. This effect is captured by the term $\mathbf{v}(z)$ in H_{1D} given in Eq. (1) and is strongly enhanced in hole nanostructures, where the SOIs are large and cause full spin rotations in lengths of a few tens of nanometers [15,18,76–78]. We show here that the SOI generally produces an inhomogeneous fully rotating Zeeman field matching those analyzed in Sec. III.

To highlight the role of the SOI, we rewrite Eq. (1) as

$$H_{1D} = \frac{[p - m\mathbf{v}(z) \cdot \boldsymbol{\sigma}]^2}{2m} + U(z) + \frac{\hbar \tilde{\boldsymbol{\omega}}_B(z) \cdot \boldsymbol{\sigma}}{2} \quad (35)$$

with $U(z) = m[\omega_o^2(z - \bar{z})^2 - |\mathbf{v}(z)|^2]/2$. We remove the SOI by the exact unitary transformation

$$S = \mathcal{P} \exp\left(i\frac{m}{\hbar} \int_0^z ds\, \mathbf{v}(s) \cdot \boldsymbol{\sigma}\right), \quad (36)$$

satisfying $S^\dagger[p - m\mathbf{v}(z) \cdot \boldsymbol{\sigma}]S = p$, and where $\mathcal{P}\exp$ is the path-ordered exponential. Generally, S describes an inhomogeneous spin rotation around a local axis.

To find an explicit expression for this rotation, we restrict our analysis to the SOI of the form

$$\mathbf{v}(z) = v_s \mathbf{n}_s + \delta\mathbf{v}(z). \quad (37)$$

By introducing the SOI length $\lambda_s = \hbar/mv_s$, we find that

$$S = e^{iz\mathbf{n}_s \cdot \boldsymbol{\sigma}/\lambda_s} e^{i\boldsymbol{\phi}_s(z) \cdot \boldsymbol{\sigma}}. \quad (38)$$

For sufficiently small $\delta\mathbf{v}(z)/v_s$, i.e., the individual components of the inhomogeneous term are bounded by $m\int_0^z ds\, \delta\mathbf{v}_j(s)/\hbar < \pi$, the phases $\boldsymbol{\phi}_s(z)$ can be estimated by a second-order Magnus expansion [119] as

$$\boldsymbol{\phi}_s(z) \approx \frac{m}{\hbar} \int_0^z ds\, \delta\tilde{\mathbf{v}}(s) + \frac{m^2}{\hbar^2} \int_0^z ds \int_0^s ds'\, \delta\tilde{\mathbf{v}}(s) \times \delta\tilde{\mathbf{v}}(s') \quad (39)$$

with $\delta\tilde{\mathbf{v}}(z) = \hat{R}_s(2z/\lambda_s)\delta\mathbf{v}(z)$; $\hat{R}_s$ is a rotation matrix by the fixed SOI axis $\mathbf{n}_s$. Here, the first integral term captures the effect of a varying amplitude of the SOI, while the second term captures the first correction due to a small tilting of the vector of the SOI. We note that, for the SOI with a constant direction $\mathbf{v}(z) = v_s(z)\mathbf{n}_s$, Eq. (39) is exact and the second integral vanishes.

Projecting the transformed Hamiltonian onto the moving charge state of the quantum dot $|\psi(z - \bar{z})|^2$, we find a spin model $H_Z = \hbar \boldsymbol{\omega}_B[\bar{z}(t)] \cdot \boldsymbol{\sigma}/2$, analogous to Eq. (2), with effective Zeeman field

$$\boldsymbol{\omega}_B[\bar{z}] = \int dz |\psi(z - \bar{z})|^2 \hat{R}_{\delta(z)}[\boldsymbol{\phi}_s(z)] \hat{R}_s[2z/\lambda_s] \tilde{\boldsymbol{\omega}}_B(z), \quad (40)$$

where $\boldsymbol{\phi}_s(z) = \phi_s(z)\delta\mathbf{n}(z)$; matrix $\hat{R}_{\delta(z)}$ describes a general rotation around the local axis $\delta\mathbf{n}(z)$. We now examine different cases. To highlight the effect of the SOI, we restrict ourselves to the analysis of a homogeneous Zeeman field, and we consider an homogeneous Zeeman field $\tilde{\boldsymbol{\omega}}_B(z) = \tilde{\boldsymbol{\omega}}_B$.

A. Spin precession in a homogeneous SOI

We first consider the homogeneous SOI

$$\mathbf{v}_H(z) = v_s \mathbf{n}_s. \quad (41)$$

The effective Zeeman field then reduces to [88]

$$\boldsymbol{\omega}_B(z) = \tilde{\boldsymbol{\omega}}_B^{\parallel} + e^{-l^2/\lambda_s^2}\hat{R}_s(2z/\lambda_s)\tilde{\boldsymbol{\omega}}_B^{\perp}, \quad (42)$$

where $\tilde{\boldsymbol{\omega}}_B^{\perp,\parallel}$ are the components of the Zeeman field perpendicular and parallel to $\mathbf{n}_s$, respectively.

If the SOI and Zeeman vectors are aligned [$\mathbf{n}_s \parallel \tilde{\boldsymbol{\omega}}_B$ and $\boldsymbol{\omega}_B(z) = \tilde{\boldsymbol{\omega}}_B^{\parallel}$], the spin rotates around a fixed axis and the noise filter function reduces to F_{FID} in Eq. (13), as discussed in Sec. III C 1. In contrast, if the SOI and Zeeman vectors are perpendicular to each other [$\mathbf{n}_s \perp \tilde{\boldsymbol{\omega}}_B$ and $\boldsymbol{\omega}_B(z) = e^{-l^2/\lambda_s^2}\hat{R}_s(2z/\lambda_s)\tilde{\boldsymbol{\omega}}_B^{\perp}$], the spin precesses around an effective Zeeman field rotating around a fixed axis in analogy to $\boldsymbol{\omega}_B^P$ in Eq. (17); see Sec. III C 2. In this case, the period of the rotation of the effective Zeeman field is determined by the SOI length λ_s; the dynamics of the spin is then given by the time-evolution operator U_Z^P in Eq. (18).

However, because of the transformation S in Eq. (38), the response of the system to noise differs from the one discussed in Sec. III. In this case, there is an important difference between global and local noise sources. For the global noise modeled by H_N in Eq. (4), the transformation S rotates the global stochastic vector $\mathbf{h}$ as $\mathbf{h} \rightarrow e^{-l^2/\lambda_s^2}\hat{R}_s(2\bar{z}/\lambda_s)\mathbf{h}$. Because this additional rotation compensates for the spin dynamics, the low-frequency noise is not filtered out and $F = e^{-2l^2/\lambda_s^2}F_{FID}$. This change results in the rescaling of the dephasing time $T_\varphi \rightarrow T_\varphi e^{l^2/\lambda_s^2}$, i.e., the dephasing time is increased inverse proportionally to the Zeeman energy renormalization; see Eq. (17).

In contrast, for local noise sources, H_N^L in Eq. (28) transforms as $\mathbf{h}_k \rightarrow \hat{R}_s(2z_k/\lambda_s)\mathbf{h}_k$. Because the rotations

in this case are local, the noise response of this system is described by the longitudinal filter function F_P^L in Eq. (29), resulting in the average shuttling fidelity $\bar{\mathcal{F}}_P^L$ given in Eq. (31). We stress that state-of-the-art experiments in hole spin qubits report $\lambda_s \sim 10$–100 nm [15,18,76,78]; thus, in analogy to the estimation in Sec. III D, we estimate a SOI-induced enhancement of the decay time T_φ^L of an order of magnitude. More details on this different noise response, including a general derivation for intermediate-range noise, are provided in Appendix C.

B. Spin nutation in an inhomogeneous SOI

Our general theory describes small variations of the SOI direction during shuttling. Such variations can arise in hole nanostructures in, for example, planar germanium and silicon fin field-effect transistors because of gate-induced strain and electric field modulations that can impact the amplitude and direction of the SOI field [81–85]. These variations are captured by the additional phases $\boldsymbol{\phi}_s$ in the transformation S; see Eq. (39). To illustrate this effect, we consider a concrete example where the SOI precesses as

$$\mathbf{v}_N(z) = v_s \left[\mathbf{n}_1 - A \sin\left(\frac{2z}{\lambda_N}\right) \mathbf{n}_2 + A \cos\left(\frac{2z}{\lambda_N}\right) \mathbf{n}_3 \right]. \tag{43}$$

The precession of the SOI has a largely different effect than the precession of the inhomogeneous Zeeman field in Eq. (22).

By using Eq. (39), we find that, when $A \ll 1$, the inhomogeneous SOI leads to the phases

$$\boldsymbol{\phi}_s \approx \frac{A^2 [\sin(2kz) - 2kz]}{4k^2\lambda_s^2} \mathbf{n}_1 - \frac{A \sin^2(kz)}{k\lambda_s} \mathbf{n}_2$$
$$+ \frac{A \sin(2kz)}{2k\lambda_s} \mathbf{n}_3, \tag{44}$$

where we define the wave vector $k = 1/\lambda_s + 1/\lambda_N$. This equation remains rather accurate for large values of $z \lesssim 1/kA^2$, as we show in Fig. 5(a) by comparing this approximation to the numerical integration of the path-ordered exponential in Eq. (36).

We focus on the homogeneous Zeeman field $\tilde{\omega}_B = \tilde{\omega}_B \mathbf{n}_3$ that is perpendicular to the constant component of the SOI. For simplicity, we now restrict ourselves to the case $\lambda_s = \lambda_N$; we lift this fine-tuned condition later. From Eq. (40), we find the effective Zeeman energy

$$\boldsymbol{\omega}_B^N(\bar{z}) = \omega_B \hat{R}_1\left(\frac{2\bar{z}}{\lambda}\right) + \delta\boldsymbol{\omega}_B(\bar{z}),$$

$$\frac{\delta\boldsymbol{\omega}_B(\bar{z})}{\omega_B} \approx \frac{A^2\bar{z}}{2k\lambda_s^2}[\cos(2\bar{z}/\lambda_s)\mathbf{n}_2 + \sin(2\bar{z}/\lambda_s)\mathbf{n}_3]. \tag{45}$$

The first term in $\boldsymbol{\omega}_B^N$ is equivalent to $\boldsymbol{\omega}_B^P$ in Eq. (17) and includes both the renormalization of the Zeeman energy
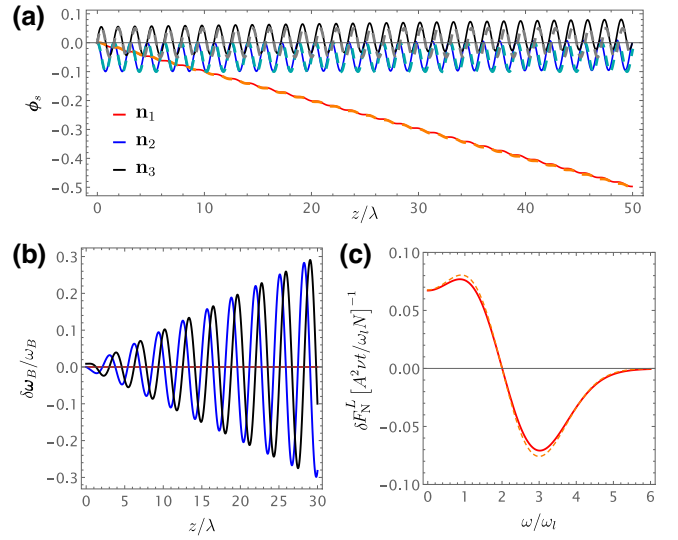

FIG. 5. Inhomogeneous SOI. (a) Inhomogeneous accumulated phases $\boldsymbol{\phi}_s$ defining the transformation S in Eq. (38). We consider here the inhomogeneous SOI $\mathbf{v}_N$ in Eq. (43) and we show with red, blue, and black curves the $\mathbf{n}_1$, $\mathbf{n}_2$, and $\mathbf{n}_3$ components of $\boldsymbol{\phi}_s$, respectively. Solid (dashed) lines represent the exact (approximate) solution obtained by discretizing Eq. (36) [from Eq. (44)]. We use $A = 0.2$ and $\lambda_s = \lambda_N = l$. (b) Variation of the effective Zeeman field $\delta\boldsymbol{\omega}_B$ caused by the inhomogeneous SOI. We show here the solution obtained by combining Eqs. (40) and (44); however, we note that the simpler approximation provided in Eq. (45) accurately reproduces the behavior of $\delta\boldsymbol{\omega}_B$. The color code and parameters used are the same as in (a). (c) Correction of the filter function for local noise sources. We show with solid and dashed lines the exact and approximate [Eq. (46)] solutions of the longitudinal filter function evaluated at $t = 20/\omega_l$.

$\omega_B = e^{-l^2/\lambda_s^2} \tilde{\omega}_B$ and the SOI-induced rotation $\hat{R}_s = \hat{R}_1$. The correction to the effective field $\delta\boldsymbol{\omega}_B$ arising from the precession of the SOI vector is shown in Fig. 5(b). We note that the largest correction originates from the term $\propto \bar{z}\mathbf{n}_1$ in $\boldsymbol{\phi}_s$ in Eq. (44), which increases linearly with $\bar{z}$, and produces the simple approximate expression provided in Eq. (45).

Focusing on local noise sources, the additional local rotation of the Zeeman field $\delta\boldsymbol{\omega}_B$ caused by the inhomogeneity of the SOI modifies the longitudinal filter function as

$$F_N^L = F_P^L + \delta F_N^L,$$

$$\delta F_N^L = \frac{A^2 vt}{4\omega_l k\lambda_s^2 N} \left[f_G'\left(\frac{\omega - 2\omega_\lambda}{\omega_l}\right) - f_G'\left(\frac{\omega + 2\omega_\lambda}{\omega_l}\right) \right], \tag{46}$$

where F_P^L is given in Eq. (30), the frequency shift $\omega_\lambda = \bar{v}/\lambda_s$, and have we introduced the first derivative of the function f_G as $f_G'(x) = -xe^{-x^2/2}$.

We show the variation δF_N^L of the filter function caused by the inhomogeneous SOI in Fig. 5(c). Compared to the homogeneous SOI case, F_N^L acquires only a small correction that scales with A^2 and is centered at $\omega \pm 2\omega_\lambda$. Interestingly, because of the linear increase of the Zeeman field $\propto \bar{z}$, the Gaussian shape of the peaks is modified by a polynomial correction. We anticipate that a similar polynomial renormalization also appears when the moving spin is resonantly driven, as we discuss in Sec. V below. We note that the corrections caused by the SOI precession are negligible in the regime considered. In contrast to the case of the precessing Zeeman field and global noise discussed in Sec. III C 3, they only quantitatively renormalize the exponential decay of the shuttling fidelity. In particular, the SOI precession renormalizes the decay rate as

$$\frac{1}{T_\varphi^L} \rightarrow \frac{1}{T_\varphi^L}\left(1 + \frac{A^2 l^2}{k\lambda_s^3}\right) = \frac{1}{T_\varphi^L}\left(1 + \frac{A^2 l^2}{2\lambda_s^2}\right), \quad (47)$$

where T_φ^L is defined in Eq. (31).

We now examine the case $\lambda_s \neq \lambda_N$; the inhomogeneous Zeeman field $\boldsymbol{\omega}_B^N$ in Eq. (45) acquires the additional correction

$$\frac{A\tilde{\omega}_B}{2k\lambda_s}[e^{-l^2/\lambda_N^2}\cos(2\bar{z}/\lambda_N) - e^{-l^2/\lambda_s^2}\cos(2\bar{z}/\lambda_s)]\mathbf{n}_1, \quad (48)$$

which is linear in A and is aligned to the homogeneous SOI direction. This term causes extra peaks in the longitudinal filter function

$$\delta F_N^L = \frac{A^2 t v}{16\omega_l k\lambda_s^2 N}\left[f_G\left(\frac{\omega \pm 2\omega_N}{\omega_l}\right) - f_G\left(\frac{\omega \pm 2\omega_\lambda}{\omega_l}\right)\right] \quad (49)$$

with $\omega_N = \bar{v}/\lambda_N$. These peaks are qualitatively similar to those in F_P^L given in Eq. (30), and only provide an additional correction to the decay rate $\propto A^2$.

V. RESONANT DYNAMICAL DECOUPLING

The average shuttling fidelity can be further enhanced by appropriately engineering the trajectory of the spin while shuttled. As anticipated, by rendering the quantum dot motion nonadiabatic with respect to the Zeeman field, but still slow compared to the orbital splitting, the resonantly induced deterministic spin dynamics more effectively filter out the low-frequency noise, thus resulting in higher shuttling fidelities. In particular, we propose two different approaches: a fast time modulation of the position of the quantum dot, and a fast shuttling in a weakly inhomogeneous Zeeman field. In these cases, one effectively obtains a resonantly driven two-level system, resulting in longer decay times and improved shuttling fidelity [18,86,120].

In this section, we restrict our analysis to shuttling experiments where the spin moves in a precessing inhomogeneous Zeeman field and focus on local noise sources. As discussed in Sec. IV, this case is equivalent to a system with a homogeneous SOI.

A. Fast time-modulated position

1. General solution

We consider a time-modulated position of the quantum dot

$$\bar{z}(t) = \bar{v}t + Z\cos(\omega_d t), \quad (50)$$

which is modulated with an additional signal with amplitude Z and frequency ω_d. We restrict to small resonant modulation with $Z \ll l$ and $\omega_d \sim \omega_B$. This additional driving term in the spin position can be experimentally achieved by appropriately designing the ac pulses of a conveyer-mode shuttler, and could be implemented in electronic systems with nanomagnets and in hole nanostructures.

The additional small driving term induces resonant dynamics in the spin degrees of freedom, thus lifting the adiabaticity condition compared to the Zeeman energy discussed in Sec. III; however, because $\omega_B \ll \omega_o$, we still consider the motion to be adiabatic compared to the orbital degree of freedom, such that the system is well described by Hamiltonian H_Z in Eq. (2). Because of the fast modulation, however, the adiabatic time evolution operator U_Z provided in Eq. (3) does not accurately describe the time evolution of H_Z. In this case, the dynamical term $i\hbar U_Z^\dagger \partial_t U_Z$, neglected in the adiabatic time evolution discussed in Sec. III, becomes relevant and induces additional resonant spin dynamics.

By applying the transformation $U_Z^{\text{TM}} = e^{-i\theta_B(\bar{z})\mathbf{n}_B(\bar{z})\cdot\boldsymbol{\sigma}/2}$ $e^{-i\omega_d t\sigma_3/2}$ to H_Z in Eq. (2), we find the effective Hamiltonian

$$H_{\text{TM}} = \frac{\hbar\Delta(\bar{z})}{2}\sigma_3 - \frac{\hbar\partial_t\bar{z}}{2}\delta\boldsymbol{\theta}_B(\bar{z})\hat{R}_3(\omega_d t)\cdot\boldsymbol{\sigma}. \quad (51)$$

For convenience, here the second transformation in U_Z^{TM} moves the system to a frame rotating at the frequency of the drive ω_d rather than at the Zeeman frequency as in U_Z in Eq. (3). We also introduce the detuning $\Delta(\bar{z}) = |\boldsymbol{\omega}_B(\bar{z})| - \omega_d$ and the vector

$$\delta\boldsymbol{\theta}_B = \theta_B'\mathbf{n}_B + \theta_B(\mathbf{n}_B \cdot \mathbf{n}_B')\mathbf{n}_B + \sin(\theta_B)(\mathbf{n}_B \times \mathbf{n}_B') \times \mathbf{n}_B$$
$$+ [1 - \cos(\theta_B)](\mathbf{n}_B \times \mathbf{n}_B'), \quad (52)$$

which is derived by using Eq. (B5) in Appendix B and the equality $e^{-X}(\partial_t e^X) = \int_0^1 ds\, e^{-sX}(\partial_t X)e^{sX}$.

We point out that corrections to Hamiltonian H_Z in Eq. (2) caused by orbital nonadiabaticity are derived in

Appendix A. In particular, for fast shuttling, one obtains the additional term $\hbar \partial_t \bar{z} \partial_{\bar{z}} \boldsymbol{\omega}_B \cdot \boldsymbol{\sigma}/2\omega_o$. For largely inhomogeneous fields, such that $\partial_{\bar{z}} \boldsymbol{\omega}_B \sim \boldsymbol{\omega}_B/l$, we find that this term produces a small correction $\propto \partial_t \bar{z} \omega_B/l\omega_o$ to Eq. (51) that is reduced compared to the second term of H_{TM} by the small factor $\omega_B/\omega_o \ll 1$. This term can thus be safely neglected for realistic experimental conditions.

2. Resonant rotating Zeeman field

Hamiltonian (51) holds generally. However, to clearly illustrate the effect of the small additional driving in Eq. (50), we now focus for concreteness on the rotating Zeeman field $\boldsymbol{\omega}_B^{\text{P}}$ defined in Eq. (17). In this case, Hamiltonian H_{TM} simplifies as

$$\frac{H_{\text{TM}}}{\hbar} = \frac{\Delta}{2}\sigma_3 - \left[\omega_\lambda e^{-i\omega_d t} - i\frac{\Omega}{2}(1 - e^{-2i\omega_d t})\right]\sigma_+ + \text{H.c.}$$

$$\approx \frac{\Delta}{2}\sigma_3 - \frac{\Omega}{2}\sigma_2 \qquad (53)$$

with H.c. the Hermitian conjugate. Here we have defined the Rabi frequency $\Omega = \omega_d Z/\lambda \ll \omega_d$ and in the second line we have used the conventional rotating-wave approximation and neglected terms rotating at the fast frequency $\omega_d \gg \Delta, \omega_\lambda, \Omega$. We have also introduced $\sigma_\pm = \sigma_1 \pm i\sigma_2$.

The Rabi frequency Ω induces an additional rotation of the moving spin. At resonance $\Delta = 0$, the spin dynamics in the rotating frame is captured by the unitary time evolution $U_\Omega = e^{i\Omega t\sigma_2/2}$, and thus in the original frame

$$U_{\text{TM}} = e^{-i\theta_B[\bar{z}(t)]\mathbf{n}_B[\bar{z}(t)]\cdot\boldsymbol{\sigma}/2} e^{-i\omega_d t\sigma_3/2} e^{i\Omega t\sigma_2/2} e^{i\theta_B(0)\mathbf{n}_B(0)\cdot\boldsymbol{\sigma}/2}. \qquad (54)$$

The time evolution of the spin expectation values obtained starting from a spin state originally in ground state $|\downarrow\rangle$ are provided in Fig. 6(a). Even a small driving term $Z \ll l$ produces nontrivial spin dynamics, as we observe by comparing the solid and dashed curves, which correspond to the cases $Z = 0.01l$ and $Z = 0$, respectively. The spin dynamics in the resonant case presents fast oscillations with frequency ω_d weighted by envelopes oscillating at the smaller frequencies Ω and ω_λ.

This nontrivial deterministic spin dynamics also strongly modifies the response of the qubit to noise. First, with a finite Rabi driving, the dominant longitudinal component of the filter function is aligned to the $\mathbf{n}_2$ direction, thus leading to

$$F = \frac{\nu}{N} \int_0^t d\tau d\tau' e^{-[\bar{z}(\tau)-\bar{z}(\tau')]^2/2l^2} e^{i\omega(\tau'-\tau)} [\hat{R}_Z^T(\tau)\hat{R}_Z(\tau')]_{22}. \qquad (55)$$

In contrast to Eq. (11), the kernel of the integral depends on $\hat{R}_Z(t)\mathbf{n}_2 = \hat{R}_1[2\bar{z}(t)/\lambda]\hat{R}_3[\omega_d t]\mathbf{n}_2$, and oscillates at the
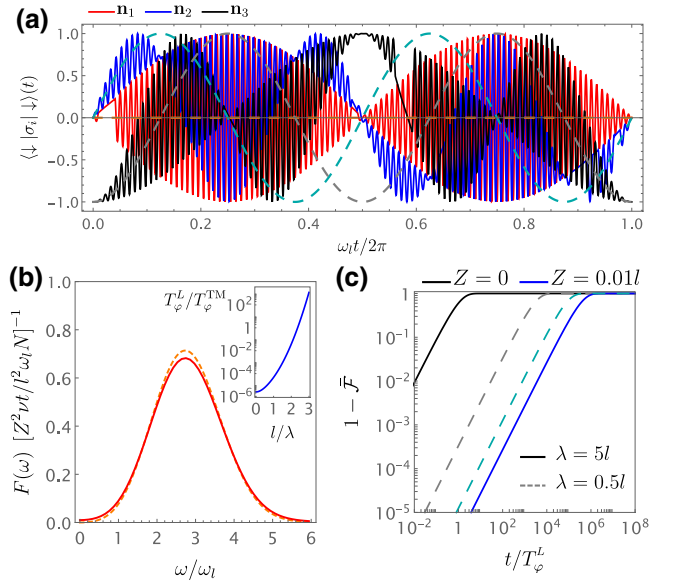

FIG. 6. Resonant dynamical decoupling with a time-modulated position. (a) Time evolution of the spin. We consider an initial spin state in $|\downarrow\rangle$, which evolves according to the unitary time-evolution operator U_{TM} in Eq. (54), and we show with red, blue, and black curves the spin expectation values aligned in the $\mathbf{n}_1$, $\mathbf{n}_2$, and $\mathbf{n}_3$ directions, respectively. Solid (dashed) lines show the case $Z = 0.01l$ ($Z = 0$). We used $\lambda = l$ and $\omega_d = 100\omega_l$. (b) Longitudinal filter function. We show here the longitudinal filter function. The solid line represents the exact solution of the integral in Eq. (55), while the dashed line is the low-frequency approximated result in Eq. (56). In the inset, we show a logarithmic plot of the rate of decay $1/T_\varphi^{\text{TM}}$ of the average shuttling fidelity against the inhomogeneity of the field l/λ; see Eq. (57). We use the same values as in (a), $t = 20/\omega_l$, and $\eta = 0.1$. (c) Average shuttling infidelity. With a double logarithmic plot we illustrate the enhanced fidelity obtained with the resonant time modulation. Solid (dashed) lines are obtained for large (small) inhomogeneities with $\lambda = 5l$ ($\lambda = 0.5l$). Blue and black lines show the fidelity with and without the additional resonant modulation, respectively. The parameters used are the same as above.

high frequency $\omega_d = \omega_B$. For this reason, one might expect F to be peaked at high frequencies. This is the case for homogeneous noise sources; however, we emphasize that the wave-function contribution $e^{-[\bar{z}(\tau)-\bar{z}(\tau')]^2/2l^2}$ also oscillates at frequency ω_d, because $\bar{z}(t)$ contains the rapidly oscillating term $\propto Z$ [see Eq. (50)], and thus F also has finite weight at low frequency, where the noise is the largest.

The exact filter function obtained by integrating Eq. (55) is shown in Fig. 6(b) with a solid red line. The integral can be performed analytically for small values of Z, but the results are lengthy and we do not report them here. However, we note that, by focusing on the dominant

low-frequency terms, F is well approximated by

$$F \approx \frac{Z^2}{l^2} \frac{\nu}{N} \frac{t}{8\omega_l} \frac{\omega^2}{\omega_l^2} \left[f_G\left(\frac{\omega - 2\omega_\lambda}{\omega_l} \right) + f_G\left(\frac{\omega + 2\omega_\lambda}{\omega_l} \right) \right]; \tag{56}$$

see the dashed orange line in Fig. 6(b). Importantly, because of the resonant dynamical decoupling, the low-frequency noise is efficiently filtered out by the additional polynomial factor ω^2 in the filter function.

The polynomial factor ω^2 in F yields the exponential decay of the average shuttling fidelity

$$\bar{\mathcal{F}}_{\mathrm{TM}} = e^{-t/T_\varphi^{\mathrm{TM}}},$$
$$T_\varphi^{\mathrm{TM}} \approx \frac{4l^2}{\eta Z^2} T_\varphi^L \left[1 + \sqrt{2\pi} \frac{l}{\lambda} e^{2l^2/\lambda^2} \mathrm{erf}\left(\frac{\sqrt{2}l}{\lambda} \right) \right]^{-1}. \tag{57}$$

Compared to the case with $Z = 0$ where the time scale is T_φ^L in Eq. (31), T_φ^{TM} is substantially enhanced by the large factor $l^2/\eta Z^2 \gg 1$. The dependence of the time constant T_φ^{TM} on the inhomogeneity of the field l/λ is illustrated in the inset of Fig. 6(b). Strikingly, the decay time T_φ^{TM} is significantly larger than T_φ^L when the Zeeman field is not strongly inhomogeneous $l/\lambda \lesssim 1$, but it becomes smaller at $l/\lambda \gtrsim 1$.

The enhancement in the average shuttling fidelity induced by the time modulation of the position can be clearly observed in Fig. 6(c) by comparing the black and blue curves. At small values of l/λ (solid lines), there is a substantial improvement in the coherence of the shuttling process that is due to the resonant dynamical decoupling induced by Z. In contrast to the $Z = 0$ case, where $l/\lambda \gtrsim 1$ is required to filter out low-frequency noise (dashed lines), the time modulation also enables a high shuttling fidelity in the regime where the Zeeman energy is weakly renormalized by the factor e^{-l^2/λ^2}.

We also note that the high-frequency components of F in Eq. (55) produce the additional high-frequency terms

$$F_{\mathrm{HF}} \approx \frac{\nu}{N} \frac{t}{2\omega_l} \left[f_G\left(\frac{\omega - \omega_B}{\omega_l} \right) + f_G\left(\frac{\omega + \omega_B}{\omega_l} \right) \right], \tag{58}$$

whose functional form resembles Eq. (30), but with shifted frequency $2\omega_\lambda \to \omega_B$. These corrections modify the fidelity as $\bar{\mathcal{F}}_{\mathrm{TM}} \to \bar{\mathcal{F}}_{\mathrm{TM}} e^{-t/T_\varphi^B}$, with time constant $T_\varphi^B = T_\varphi^L e^{-2l^2/\lambda^2 + \omega_B^2/\omega_l^2} \gg T_\varphi^{\mathrm{TM}}$ for small values of $\omega_l/\omega_B \ll 1$.

3. Finite detuning and phase driving

A homogeneous detuning Δ in H_{TM} in Eq. (53) tilts the Rabi rotation by an angle $\varphi = \arctan(\Delta/\Omega)$ around the $\mathbf{n}_1$ axis and speeds up the Rabi frequency by $\Omega \to$

$\sqrt{\Omega^2 + \Delta^2}$. The detuning causes incomplete Rabi oscillations with probability $P = \Omega^2/(\Omega^2 + \Delta^2)$ and the typical Rabi chevron pattern measured in Rabi experiments. Assuming a large driving field Ω compared to Δ, the angle $\varphi \approx \Delta/\Omega \ll 1$ causes the appearance of a competing decay time for the average shuttling fidelity in Eq. (57) that modifies as $\bar{\mathcal{F}}_{\mathrm{TM}} \to \bar{\mathcal{F}}_{\mathrm{TM}} e^{-t/T_\varphi^\Delta}$, with

$$T_\varphi^\Delta \approx T_\varphi^L/\varphi^2 + \mathcal{O}(\varphi^3), \tag{59}$$

where the decay time T_φ^L of adiabatic shuttling is given in Eq. (31).

First, comparing T_φ^Δ to T_φ^{TM}, we find that T_φ^Δ dominates when the Zeeman field is largely inhomogeneous $l/\lambda \gtrsim 1$ and when the power spectrum $S(\omega)$ of the noise strongly deviates from the $1/|\omega|$ trend, i.e., at large values of η in Eq. (14). However, even in this case, we emphasize that sufficiently close to resonance ($\varphi \ll 1$) $T_\varphi^\Delta \gg T_\varphi^L$, thus showing that time modulation provides a substantial advantage compared to adiabatic driving.

We also point out that an inhomogeneous detuning $\Delta(\bar{z})$, which can originate in experiments from local modulations of the g factor or the magnetic fields, in general only results in an additional small correction to the fidelity in Eq. (59). In particular, we focus here on the detuning

$$\Delta[\bar{z}(t)] = \Delta_0 + \Delta_1 \cos\left[\frac{2\bar{z}(t)}{\lambda_\Delta} \right] \approx \Delta_0 + \Delta_1 \cos(2\omega_\Delta t), \tag{60}$$

where we have introduced $\omega_\Delta = \bar{v}/\lambda_\Delta$ and $\Delta_0 = \omega_B - \omega_d$, with ω_B the average Zeeman energy during shuttling.

With this inhomogeneous detuning, Hamiltonian H_{TM} in Eq. (53) is modified to the phase driving Hamiltonian [86]

$$H_{\mathrm{PD}} \approx \frac{\hbar\omega_B}{2}\sigma_3 + \frac{\hbar\Delta_1}{2}\cos(2\omega_\Delta t)\sigma_3 - \hbar\Omega\sin(\omega_d t)\sigma_1, \tag{61}$$

where the driving field has two tones and couples to the transversal (Rabi driving $\propto \Omega\sigma_1$) and longitudinal (phase driving $\propto \Delta_1\sigma_3$) spin degrees of freedom. For clarity, here we report the Hamiltonian before performing the rotating frame transformation $e^{-i\omega_d t\sigma_3/2}$ of U_Z^{TM}, i.e., without the rotation $\hat{R}_3(\omega_d t)$ in H_{TM}; see Eq. (51).

As demonstrated in Ref. [86], in general cases only off-resonant phase driving, with frequency $\omega_\Delta \sim \Omega$, significantly impacts the spin dynamics. For this reason, in Eq. (60), we discarded fast rotating phase driving terms oscillating at frequencies ω_d. In contrast, Rabi driving only impacts the spin dynamics when close to resonance $\omega_d \sim \omega_B$, and for this reason, we neglect slowly rotating Rabi driving terms oscillating at frequencies ω_l.

For small values of the modulation $\Delta_1 \lesssim \omega_\Delta$, the effect of phase driving is negligible and one can safely operate

at $\Delta_0 = 0$, i.e., by using a microwave pulse resonant with the average of the inhomogeneous Zeeman energy ω_B. For larger values of $\Delta_1 \gtrsim \omega_\Delta$, phase driving introduces additional interesting dynamics in the spin evolution [86]. First, operating at a finite Δ_0 enables additional resonant dynamics of the spin at $\Delta_0 = \pm 2m\omega\Delta$, with integer m, where the Rabi frequency is rescaled by $\Omega J_m(\Delta_1/\omega_\Delta)$. Here $J_m(x)$ is the mth Bessel function. This additional resonant dynamics will also effectively filter out low-frequency noise. Moreover, as discussed in Ref. [86], even for small values of $\Delta_1 \lesssim \omega_\Delta$, by fine-tuning the Rabi frequency to $\Omega \sim 2\omega_\Delta$, we expect that additional resonant dynamics could substantially enhance the filtering out of dominant noise sources, further improving the average shuttling fidelity.

4. Precessing Zeeman field

Finally, we discuss the role of a precessing Zeeman field when the position is time modulated. These effects can be nicely described by our theory and in particular by H_{TM} in Eq. (51). By considering for concreteness the precessing Zeeman field ω_B^N in Eq. (21) that enables spin nutation, and using Eq. (52), we find that, for small values of A, the driving term in H_{TM} modifies as

$$\delta\boldsymbol{\theta}_B = \frac{2}{\lambda}\left[\mathbf{n}_1 - A\sin\left(\frac{4\bar{z}}{\lambda}\right)\mathbf{n}_2 + A\cos\left(\frac{4\bar{z}}{\lambda}\right)\mathbf{n}_3\right] + \mathcal{O}(A^2),$$

(62)

where we only kept the terms to linear order in A, and we restrict ourselves to the analysis of the case $\lambda = \lambda_N$.

In this case, there are two leading corrections to the spin dynamics. In particular, we note that the last contribution in the expansion gives rise to a phase driving, see Eq. (61), with frequency $4\omega_\lambda$ and amplitude $2\omega_\lambda A$. As argued in Sec. V A 3, for small values of A and far from the fine-tuned resonance condition $4\omega_\lambda \sim \Omega$, this term has negligible effect.

Moreover, the transversal term comprises a far detuned pulse with frequency $4\omega_\lambda$ that does not significantly contribute to the spin dynamics and the frequency-modulated nearly resonant term $-\omega_d A Z \sin(\omega_d t)\sin(4\omega_\lambda t)$. In the rotating-wave approximation, this term yields an additional transversal Rabi driving. When off resonant and $\Omega \gg 4\omega_\lambda$, this term is negligible and thus we do not explore it further in this work. Interestingly, however, we envision that this frequency-modulated driving could provide an additional effective filtering of the noise, which is analogous to the frequency modulation in sinusoidally modulated, always rotating and tailored dressed qubit protocols in global fields [120–122]. An optimized pulse shaping could also further enhance the fidelity [123–126].

B. Fast shuttling in weakly inhomogeneous fields

In Sec. III C, we showed that a fully rotating Zeeman field enables an effective way to intrinsically dynamically decouple a shuttled spin from low-frequency noise, thus resulting in a high shuttling fidelity. In particular, we focused on particles moving adiabatically with a constant velocity $\bar{v} \ll |\omega_B|l \ll \omega_o l$, which is small compared to both Zeeman and orbital energies. We also demonstrated in Sec. V A that the shuttling fidelity can be further improved by adding a small time-dependent modulation that is nonadiabatic with respect to $|\omega_B|$, but still adiabatic compared to ω_o. Here, we show that a substantial improvement in fidelity also occurs for incomplete rotations of the Zeeman field, when the constant shuttling velocity is nonadiabatic compared to the Zeeman field $|\omega_B|$, but remains adiabatic compared to ω_o.

For concreteness, we consider the weakly inhomogeneous Zeeman field

$$\boldsymbol{\omega}_B^D(\bar{z}) = \omega_B\left[A\cos\left(\frac{2\bar{z}}{\lambda}\right)\mathbf{n}_1 + A\sin\left(\frac{2\bar{z}}{\lambda}\right)\mathbf{n}_2 + \mathbf{n}_3\right]$$

(63)

with $A \ll 1$ and a constant velocity motion with $\bar{z} = \bar{v}t$. This Hamiltonian accurately describes a residual homogeneous magnetic field in electronic systems with nanomagnets [99] and hole heterostructures, for example in planar germanium, presenting an incomplete tilting of the g tensor [70].

When $\bar{v}$ is adiabatic compared to the Zeeman field $\bar{v} \ll \omega_B l$, the shuttling fidelity is dominated by the dephasing accumulated by the homogeneous component of the Zeeman field aligned along $\mathbf{n}_3$; see Sec. III C. However, here we focus instead on a different case, where $\bar{v} \sim \omega_B l$, and show that in this case there are resonant conditions for $\bar{v}$ that can substantially filter out low-frequency noise, still providing a large enhancement in the shuttling fidelity. We note that, as derived in Appendix A, corrections to Eq. (2) arising from possible orbital nonadiabaticity are $\propto A\omega_\lambda\omega_B/\omega_o$ with $\omega_\lambda = \bar{v}/\lambda$ and remain negligible compared to the leading terms $\propto A\omega_B$ also in this case because they are suppressed by the small parameter $\omega_B/\omega_o \ll 1$.

The resonance condition in this case is straightforwardly recognizable by moving to a rotating frame with frequency $2\omega_\lambda$ via the transformation $e^{-i\omega_\lambda t\sigma_3}$. In this frame, we immediately recognize the time-independent Rabi Hamiltonian

$$H_{\mathrm{D}} = \frac{\hbar\Delta}{2}\sigma_3 + \frac{\hbar\Omega}{2}\sigma_1, \qquad \Omega = A\omega_B, \ \Delta = \omega_B - 2\omega_\lambda,$$

(64)

describing the Rabi oscillation of the spin with Rabi frequency Ω at resonance $\Delta = 0$; see also Eq. (53).

We now focus on local noise sources and we can straightforwardly verify that the longitudinal component

of the filter function F_D^L is equivalent to F_P^L that is given in Eq. (30). We then find the shuttling fidelity

$$\bar{\mathcal{F}}_\mathrm{D}^L \approx e^{-t/T_\varphi^L}, \qquad T_\varphi^L = \omega_l \left(\sqrt{\frac{N}{\nu}} T_\varphi \right)^2 e^{2l^2/\lambda^2}. \quad (65)$$

This result is equivalent to Eq. (31); however, we emphasize that because in this case the Zeeman field is not fully rotating, the Zeeman energy ω_B is not rescaled by the small prefactor e^{-l^2/λ^2}. As a result, at large values of the ratio $l/\lambda \gtrsim 1$ the Zeeman energy remains large, while the fidelity is rapidly improved. This critical difference between this approach and that in Sec. III C is clearly illustrated by comparing the dashed and solid gray lines in Fig. 5(b), corresponding to the Zeeman fields in the two situations, which yield the same shuttling fidelity (blue line).

We stress that the condition $\Delta = 0$ is within the reach of state-of-the-art experiments. If we consider the experimentally realistic value $\pi\lambda = 50$ nm, achievable in electronic systems by nanomagnets [99] and corresponding in hole systems to the gate spacing that determines the tilt of the g tensor [6,70], we find that, for the typical value $\omega_B/2\pi = 1$ GHz, high-fidelity shuttling can be achieved at realistic velocities $\bar{v} = \omega_B\lambda/2 = 50$ m/s [73]. Our protocol thus enables at the same time high-fidelity and fast shuttling even in the presence of residual large homogeneous Zeeman fields.

VI. CONCLUSION

In this work, we showed that the fidelity of the spin shuttling can be substantially enhanced by engineering highly inhomogeneous Zeeman fields. We related this surprising effect to the nontrivial deterministic dynamics of the spin during its motion, which filters out the dominant low-frequency components of the noise. This intrinsic dynamical decoupling of low-frequency noise is a general feature that appears in a wide variety of relevant experimental cases, including hole nanostructures in silicon and germanium as well as in electronic systems with artificial spin-orbit fields induced by micromagnets. We propose a framework to describe many scenarios where spins are shuttled in an inhomogeneous Zeeman field caused by rotation of principal axes of g tensors, inhomogeneous magnetic fields, and SOIs. We also include a detailed analysis of different sources of noise that affect the shuttled spin in a global or local way. The findings of this work are summarized in Table I.

Despite some qualitative and quantitative differences in these cases, we confirm that an inhomogeneous Zeeman field improves the shuttling fidelity independent of the noise locality. We also propose protocols where the spin is moved nonadiabatically compared to the Zeeman energy that enable further dynamical decoupling of low-frequency noise and can thus significantly improve the coherence of shuttling. Our findings clearly demonstrate that highly efficient shuttling can be reached in materials with large SOI and inhomogeneous Zeeman fields, and that these systems are not only ideal hosts for compact spin-qubit architectures, but also for long-range spin qubit connectivity, and are thus ideal candidates for future large-scale quantum computers.

ACKNOWLEDGMENTS

APPENDIX A: NONADIABATIC CORRECTIONS

We now discuss in more detail the condition of adiabaticity of the quantum dot motion compared to the orbital

TABLE I. Summary of the shuttling fidelity for the main examples in each section for global and local noise sources. Corrections and additional scenarios are discussed in the main text.

	Adiabatic motion compared to the Zeeman field (Secs. III and IV)		
	FID (Sec. III C 1)	Inhomogeneous field (Sec. III C 2)	SOI (Sec. IV A)
$\boldsymbol{\omega}_B(t)/\tilde{\omega}_B$	$\mathbf{n}_3$	$e^{-l^2/\lambda^2}\hat{R}_1(2\omega_\lambda t)\mathbf{n}_3$	$e^{-l^2/\lambda_s^2}\hat{R}_1(2\omega_s t)\mathbf{n}_3$
$\bar{\mathcal{F}}_\mathrm{global}$	e^{-t^2/T_φ^2} [Eq. (15)]	$\begin{cases} e^{-t^2 f_L(\omega_\lambda t)/T_\varphi^2}, & t \lesssim T_\mathrm{P} \\ e^{-t/T_\mathrm{P}}, & t \gtrsim T_\mathrm{P} \end{cases}$ [Eq. (20)]	e^{-t^2/T_φ^2}
$\bar{\mathcal{F}}_\mathrm{local}$	$e^{-\nu t^2/NT_\varphi^2}$	e^{-t/T_φ^L} [Eq. (31)]	e^{-t/T_φ^L}
	Nonadiabatic motion compared to the Zeeman field (Sec. V)		
	FID (Sec. III C 1)	Time modulation of the position (Sec. V A)	Resonant (Sec. V B)
$\boldsymbol{\omega}_B(t)/\tilde{\omega}_B$	$\mathbf{n}_3$	$e^{-l^2/\lambda^2}\hat{R}_1[2\omega_\lambda t + 2Z\cos(\omega_B t)/\lambda]\mathbf{n}_3$	$[1 + A\hat{R}_1(2\omega_B t)]\mathbf{n}_3$
$\bar{\mathcal{F}}_\mathrm{local}$	$e^{-\nu t^2/NT_\varphi^2}$	$e^{-t/T_\varphi^\mathrm{TM}}$ [Eq. (57)]	e^{-t/T_φ^L} [Eq. (65)]

degrees of freedom. We stress again that in the main text, we occasionally lift the condition of adiabaticity compared to the Zeeman field $\omega_B/2\pi \lesssim 10$ GHz, but the shuttling is always adiabatic compared to the orbital splitting $\omega_o/2\pi \gtrsim 1$ THz. First, we derive with a simple perturbative treatment the expected corrections to the model presented in the main text, and then we verify these corrections by showing that they match an exactly solvable simple case.

1. Perturbative treatment

Our derivations in the main text always assume that the quantum dot motion remains adiabatic compared to the

orbital degree of freedom. We now discuss the validity of this approximation by using a simple model that perturbatively includes the contribution of the next excited orbital state.

In particular, we now include in our derivation of Eq. (2) the effect of the neglected dynamical term $-ip\partial_t\bar{z}$, originating from the time dependence of state $\psi[z - \bar{z}(t)]$. The expectation value of this term in the ground state vanishes. However, this term provides a coupling to the first excited state $\psi_1[z - \bar{z}(t)]$; assuming a harmonic potential, $\psi_1(z) = H_1(z/l)e^{-z^2/2l^2}/\pi^{1/4}\sqrt{2l}$ with H_1 the first Hermite polynomial.

The effective Hamiltonian acting on these two states is

$$H = \hbar \begin{pmatrix} \boldsymbol{\omega}_B(\bar{z}) \cdot \boldsymbol{\sigma}/2 & -l\partial_{\bar{z}}\boldsymbol{\omega}_B(\bar{z}) \cdot \boldsymbol{\sigma}/2\sqrt{2} + \partial_t\bar{z}\sigma_0/\sqrt{2}l \\ -l\partial_{\bar{z}}\boldsymbol{\omega}_B(\bar{z}) \cdot \boldsymbol{\sigma}/2\sqrt{2} + \partial_t\bar{z}\sigma_0/\sqrt{2}l & \boldsymbol{\omega}_B^1(\bar{z}) \cdot \boldsymbol{\sigma}/2 + \omega_o\sigma_0 \end{pmatrix}, \tag{A1}$$

where we have introduced $\boldsymbol{\omega}_B^1(\bar{z}) = \int dz |\psi_1(z)|^2 \tilde{\boldsymbol{\omega}}_B(z + \bar{z})$. We also use the relation $\int dz \psi(z)\psi_1(z)\tilde{\boldsymbol{\omega}}_B(z + \bar{z}) = -l\partial_{\bar{z}}\boldsymbol{\omega}_B(\bar{z})/\sqrt{2}$, valid for harmonic potential eigenfunctions and straightforward to derive using the Rodrigues formula defining Hermite polynomials.

By using second-order perturbation theory, we find the effective Hamiltonian for the ground state:

$$H = \frac{\hbar}{2}\left[\boldsymbol{\omega}_B(\bar{z}) + \frac{\partial_t\bar{z}}{\omega_o}\partial_{\bar{z}}\boldsymbol{\omega}_B(\bar{z})\right] \cdot \boldsymbol{\sigma}. \tag{A2}$$

The corrections arising from the orbital nonadiabaticity of the motion approximately scale as $\omega_\lambda\omega_B/\omega_o$. In our work, these corrections are most significant when we lift the Zeeman field adiabaticity condition, in which case we have approximately ω_B^2/ω_o, and they still produce small terms that are quadratic in the magnetic field.

2. Exact solution with an SOI

Here, we validate the perturbative results just derived by presenting an exact solution for the time-dependent Schrodinger equation, which fully accounts for nonadiabatic corrections. This solution describes a spin confined in a quantum dot moving in a homogeneous Zeeman aligned to a possibly time-dependent SOI field with a fixed direction.

We consider the one-dimensional Hamiltonian

$$H = \frac{p^2}{2m} + \frac{m\omega_o^2}{2}z^2 + v(t)p\sigma_3 + m\omega_o^2\bar{z}(t)z + \frac{\hbar\omega_B}{2}\sigma_3, \tag{A3}$$

where the SOI and Zeeman fields are aligned along the $\mathbf{n}_3$ direction. Introducing the usual orbital bosonic ladder operators a and $a^\dagger$, the harmonic length l, and the time-dependent spin-orbit length $\lambda_s(t) = \hbar/mv(t)$, we can rewrite this Hamiltonian as

$$\frac{H}{\hbar\omega_o} = a^\dagger a + \frac{\omega_B}{2\omega_o}\sigma_3 + \frac{il}{\sqrt{2}\lambda_s(t)}(a^\dagger - a)\sigma_z + \frac{\bar{z}(t)}{\sqrt{2}l}(a^\dagger + a). \tag{A4}$$

We move to a spin-dependent rotating frame by the unitary operator

$$U_E(t) = e^{-it(\omega_o a^\dagger a + \omega_B\sigma_3/2)}, \tag{A5}$$

yielding

$$\frac{H_R}{\hbar\omega_o} = \alpha(t)a^\dagger + \alpha^\dagger(t)a, \tag{A6a}$$

$$\alpha(t) = \frac{e^{i\omega_o t}}{\sqrt{2}}\left[\frac{\bar{z}(t)}{l} + \frac{il}{\lambda_s(t)}\sigma_3\right], \tag{A6b}$$

where we have used $U_E^\dagger(t)aU_E(t) = ae^{-i\omega_o t}$.

The time-evolution operator of the system can then be formally found as

$$U(t) = U_E(t)\mathcal{T}e^{-i\int_0^t H_R(\tau)d\tau/\hbar}. \tag{A7}$$

In our case, this equation can be evaluated exactly because the spin sector remains diagonal during the time evolution and the problem is quadratic in the orbital degree of freedom. The explicit exact solution of the time-ordered exponential is obtained by a second-order Magnus expansion

[119], because $[a, a^\dagger] = 1$ and higher-order commutators coming from the expansions vanish and the result of the second-order expansion is exact.

We thus obtain

$$U(t) = U_E(t)e^{-i\phi(t)}D[\Gamma(t)]. \tag{A8}$$

We introduced the conventional quantum optical displacement operator $D(x) = e^{xa^\dagger - x^\dagger a}$, and the spin-dependent phase-space shift $\Gamma(t)$ and phase $\phi(t)$ are

$$\Gamma(t) = -i\omega_o \int_0^t \alpha(\tau)d\tau, \tag{A9a}$$

$$\phi(t) = i\omega_o^2 \int_0^t d\tau \int_0^\tau d\tau' \frac{\alpha(\tau)\alpha^\dagger(\tau') - \alpha^\dagger(\tau)\alpha(\tau')}{2}. \tag{A9b}$$

As a concrete example, we consider the case $\bar{z}(t) = \bar{v}t$ and a time independent λ_s, in which case

$$\Gamma(t) = -\frac{e^{i\omega_o t}}{\sqrt{2}}\left[\theta_1(t) + i\frac{l}{\lambda_s}(1 - e^{-i\omega_o t})\sigma_3\right], \tag{A10a}$$

$$\theta_1(t) = \omega_l t + i\frac{\omega_l}{\omega_o}(1 - e^{-i\omega_o t}), \tag{A10b}$$

$$\phi(t) = \phi_0 - \left[\frac{\omega_s t}{2}[1 + \cos(\omega_o t)] - \frac{\omega_s}{\omega_o}\sin(\omega_o t)\right]\sigma_3, \tag{A10c}$$

where ϕ_0 is a trivial global spin-independent phase, and $\omega_l = \bar{v}/l$ and $\omega_s = \bar{v}/\lambda_s$, as in the main text.

We focus on the time evolution of the orbital ground states of H_R at time $t = 0$ and centred at $\bar{z}(0) = 0$:

$$|\psi_{\uparrow\downarrow}\rangle_0 = D\left(-\frac{il\sigma_3}{\sqrt{2}\lambda_s}\right)|0, \tilde{\uparrow}\tilde{\downarrow}\rangle \tag{A11}$$

with the $\tilde{\uparrow}\tilde{\downarrow}$ spins the pseudospin degrees of freedom defined by removing the SOI by the usual transformation $D\left(-il\sigma_3/\sqrt{2}\lambda_s\right)$. The time-evolved state at time t is

$$|\psi_{\uparrow\downarrow}\rangle(t) = e^{-i\omega_B t\sigma_3/2 - i\phi(t)}e^{il\lambda_s \text{Re}[\Gamma(t)]\sigma_3/\sqrt{2}}$$
$$\times D\left[\left(\Gamma(t) - \frac{il}{\sqrt{2}\lambda_s}\sigma_3\right)e^{-i\omega_o t}\right]|0, \tilde{\uparrow}\tilde{\downarrow}\rangle. \tag{A12}$$

In particular, when $\bar{z}(t) = \bar{v}t$, we find that

$$|\psi_{\uparrow\downarrow}(t)\rangle = e^{-i[\omega_B t + \theta_0(t)]\sigma_3/2}D\left[-\frac{\theta_1(t)}{\sqrt{2}} - i\frac{l}{\sqrt{2}\lambda_s}\sigma_3\right]|0, \tilde{\uparrow}\tilde{\downarrow}\rangle$$
$$= e^{-i[\omega_B t + 2\theta_0(t)]\sigma_3/2}D\left[-\frac{\theta_1(t)}{\sqrt{2}}\right]D\left[-\frac{il\sigma_3}{\sqrt{2}\lambda_s}\right]|0, \tilde{\uparrow}\tilde{\downarrow}\rangle$$
$$= e^{-i[\omega_B t + 2\theta_0(t)]\sigma_3/2}D\left[-\frac{\theta_1(t)}{\sqrt{2}}\right]|\psi_{\uparrow\downarrow}\rangle_0, \tag{A13}$$

where we have introduced the spin-dependent phase shift

$$\theta_0(t) = -\omega_s t + \frac{\omega_s}{\omega_o}\sin(\omega_o t). \tag{A14}$$

In this simple case, it is clear that the nonadiabatic corrections provide fast oscillations of the angles $\theta_{0,1}(t)$ that become suppressed as $\omega_l \sim \omega_s \ll \omega_o$.

More generally, by averaging out the fast oscillations of period $1/\omega_o$, one can generalize these results as

$$\theta_0(t) \approx -\bar{z}(t)/\lambda_s \quad \text{and} \quad \theta_1(t) \approx \bar{z}(t)/l. \tag{A15}$$

As expected, we note that the nonadiabatic corrections are $\propto \omega_{l,s}/\omega_o$ and result in additional oscillation terms $\propto e^{-i\omega_o t}$ that we neglect in our adiabatic approximation.

APPENDIX B: ROTATION MATRICES

Here, we provide an explicit expression for the rotation matrices used in the main text. The unitary operator

$$U = e^{-i\theta\mathbf{n}\cdot\boldsymbol{\sigma}/2}, \tag{B1}$$

with unit vector $\mathbf{n} = (n_1, n_2, n_3)$ (such that $\mathbf{n} \cdot \mathbf{n} = 1$), transforms a vector of Pauli matrices $\boldsymbol{\sigma} = (\sigma_1, \sigma_2, \sigma_3)$ as

$$U^\dagger \boldsymbol{\sigma} U = \hat{R}_{\mathbf{n}}(\theta)\boldsymbol{\sigma}. \tag{B2}$$

The counterclockwise rotation matrix $\hat{R}_{\mathbf{n}}(\theta)$ rotates a vector by an angle θ around $\mathbf{n}$ and is given by

$$\hat{R}_{\mathbf{n}}(\theta) = \begin{pmatrix} (1-n_x^2)\cos(\theta)+n_x^2 & n_x n_y[1-\cos(\theta)]-\sin(\theta)n_z & n_x n_z[1-\cos(\theta)]+\sin(\theta)n_y \\ n_x n_y[1-\cos(\theta)]+\sin(\theta)n_z & (1-n_y^2)\cos(\theta)+n_y^2 & n_y n_z[1-\cos(\theta)]-\sin(\theta)n_x \\ n_x n_z[1-\cos(\theta)]-\sin(\theta)n_y & n_y n_z[1-\cos(\theta)]+\sin(\theta)n_x & (1-n_z^2)\cos(\theta)+n_z^2 \end{pmatrix}. \tag{B3}$$

For convenience, we also define the rotation matrices $\hat{R}_i(\theta)$ around the $i = (1, 2, 3)$ axis as

$$\hat{R}_1(\theta) = \begin{pmatrix} 1 & 0 & 0 \\ 0 & \cos(\theta) & -\sin(\theta) \\ 0 & \sin(\theta) & \cos(\theta) \end{pmatrix}, \tag{B4a}$$

$$\hat{R}_2(\theta) = \begin{pmatrix} \cos(\theta) & 0 & \sin(\theta) \\ 0 & 1 & 0 \\ -\sin(\theta) & 0 & \cos(\theta) \end{pmatrix}, \tag{B4b}$$

$$\hat{R}_3(\theta) = \begin{pmatrix} \cos(\theta) & -\sin(\theta) & 0 \\ \sin(\theta) & \cos(\theta) & 0 \\ 0 & 0 & 1 \end{pmatrix}, \tag{B4c}$$

and we report the useful relation

$$\hat{R}_{\mathbf{n}}(\theta)\mathbf{A} = \mathbf{n}(\mathbf{n} \cdot \mathbf{A}) + \cos\theta (\mathbf{n} \times \mathbf{A}) \times \mathbf{n} + \sin\theta (\mathbf{n} \times \mathbf{A}). \tag{B5}$$

For the discussion in the main text, we are particularly interested in the solution of the equation

$$\hat{R}_{\mathbf{n}}(\theta)\mathbf{n}_3 = [\sin(\varphi)\sin(\varphi_1), \sin(\varphi_1)\cos(\varphi), \cos(\varphi_1)], \tag{B6}$$

which aligns a general vector parametrized by the angles $\varphi \in [0, 2\pi)$ and $\varphi_1 \in [0, \pi)$ to the third direction. Note that rotation $\hat{R}_{\mathbf{n}}(\theta)$ is straightforwardly decomposed as $\hat{R}_{\mathbf{n}}(\theta) = \hat{R}_3(-\varphi)\hat{R}_1(-\varphi_1)$. A particular solution for the vector and angle of the combined rotations valid for $\cos(\varphi_1) \geq 0$ is

$$\theta = -\text{sgn}(\sin\varphi)\cos^{-1}\left(\frac{\cos\varphi + (1+\cos\varphi)\cos\varphi_1 - 1}{2}\right), \tag{B7a}$$

$$\mathbf{n} = \left[\cos\left(\frac{\varphi}{2}\right)\cos\left(\frac{\phi}{2}\right), -\sin\left(\frac{\varphi}{2}\right)\cos\left(\frac{\phi}{2}\right), \sin\left(\frac{\phi}{2}\right)\right], \tag{B7b}$$

$$\phi = -2\sin^{-1}\left[\tan\left(\frac{\varphi}{2}\right)\cot\left(\frac{\theta}{2}\right)\right]. \tag{B7c}$$

For small positive angles φ_1 around the third axis, one can Taylor expand this solution to the first order in φ_1,

resulting in

$$\theta = -\cos^{-1}[\cos(\varphi)]\text{sgn}[\sin(\varphi)] + \mathcal{O}(\varphi_1^2), \tag{B8a}$$

$$\phi = \pi - \frac{\varphi_1}{|\sin(\varphi/2)|} + \mathcal{O}(\varphi_1^2), \tag{B8b}$$

$$\mathbf{n} = \left[\frac{\varphi_1\text{sgn}[\sin(\varphi/2)]}{2}\cot\left(\frac{\varphi}{2}\right), \frac{-\varphi_1\text{sgn}[\sin(\varphi/2)]}{2}, 1\right], \tag{B8c}$$

or, equivalently, unwinding the phases,

$$\theta = -\varphi, \tag{B9a}$$

$$\mathbf{n} = \left[\frac{\varphi_1}{2}\cot\left(\frac{\varphi}{2}\right), -\frac{\varphi_1}{2}, 1\right] + \mathcal{O}(\varphi_1^2), \tag{B9b}$$

resulting in the vector

$$\hat{R}_{\mathbf{n}}(\theta)\mathbf{n}_3 = [\varphi_1\sin(\varphi), \varphi_1\cos(\varphi), 1] + \mathcal{O}(\varphi_1^2). \tag{B10}$$

APPENDIX C: INTERMEDIATE-RANGE NOISE SOURCES

We discuss in more detail the role of inhomogeneous noise with an intermediate range. We focus on systems with arbitrary SOI. To this end, we consider Hamiltonian H_{1D} in Eq. (35), and the noise Hamiltonian

$$H_N^z = \frac{1}{2n_0}\sum_k V(z - z_k)\mathbf{h}_k(t) \cdot \boldsymbol{\sigma}, \tag{C1}$$

where the function $V(z - z_k)$ determines whether the noise sources are local $[V(z) = \delta(z)]$ or global $[V(z) = n_0]$. Here we consider a homogeneous Zeeman field, i.e., $\tilde{\boldsymbol{\omega}}_B(z) = \tilde{\boldsymbol{\omega}}_B$.

We remove the SOI by transformation S in Eq. (38) and we project the total Hamiltonian onto the moving dot ground-state wave function, resulting in the effective Hamiltonian

$$H = \frac{\hbar\boldsymbol{\omega}_B(\bar{z}) \cdot \boldsymbol{\sigma}}{2} + \frac{1}{2}\tilde{\boldsymbol{H}}(\bar{z}, t) \cdot \boldsymbol{\sigma} \tag{C2}$$

with [see Eq. (40)]

$$\boldsymbol{\omega}_B(\bar{z}) = \tilde{\boldsymbol{\omega}}_B \int_{-\infty}^{+\infty} dz |\psi(z - \bar{z})|^2 \hat{R}_s^T[2z/\lambda_s]\hat{R}_{\delta(z)}^T[\phi_s(z)], \tag{C3a}$$

$$\tilde{\boldsymbol{H}}(\bar{z},t) = \frac{1}{n_0} \sum_k \mathbf{h}_k(t) \int_{-\infty}^{+\infty} dz V(z - z_k) |\psi(z - \bar{z})|^2$$

$$\times \hat{R}_s^T[2z/\lambda_s] \hat{R}_{\delta(z)}^T[\phi_s(z)].$$
(C3b)

The longitudinal component of the covariance matrix $\hat{\Sigma}_{33}$, which determines the average shuttling fidelity, is

$$\hat{\Sigma}_{33} = \frac{1}{2\pi\hbar^2} \int_{-\infty}^{\infty} d\omega \, \boldsymbol{\eta}^\dagger(\omega,t) \hat{S}(\omega) \boldsymbol{\eta}(\omega,t)$$
(C4)

with $\hat{S}_{ij}(\omega) = \int dt e^{i\omega t} \langle h_i(t) h_j(0) \rangle$ a general anisotropic noise spectral function. We introduced the vector

$$\boldsymbol{\eta} = \frac{1}{n_0} \int_0^t d\tau e^{-i\omega\tau} \sum_k \int_{-\infty}^{+\infty} dz V(z - z_k) |\psi[z - \bar{z}(\tau)]|^2$$

$$\times \hat{R}_s^T[2z/\lambda_s] \hat{R}_{\delta(z)}^T[\phi_s(z)] \frac{\boldsymbol{\omega}_B[\bar{z}(\tau)]}{|\boldsymbol{\omega}_B[\bar{z}(\tau)]|}.$$
(C5)

Assuming isotropic uncorrelated noise, $\hat{S}_{ij}(\omega) = \delta_{ij} S(\omega)$, we find that the longitudinal filter function is $\hat{F}_{33} = F = \boldsymbol{\eta}^\dagger \cdot \boldsymbol{\eta}$.

For global and local noise, we respectively obtain

$$\tilde{\boldsymbol{H}}_G = \mathbf{h} \int_{-\infty}^{+\infty} dz |\psi(z - \bar{z})|^2 \hat{R}_s^T[2z/\lambda_s] \hat{R}_{\delta(z)}^T[\phi_s(z)],$$

and $\quad \tilde{\boldsymbol{H}}_L = \frac{1}{n_0} \sum_k |\psi(z_k - \bar{z})|^2 \mathbf{h}_k \hat{R}_s^T[2z_k/\lambda_s] \hat{R}_{\delta(z_k)}^T[\phi_s(z_k)].$
(C6)

Here we define $\mathbf{h} = \sum_k \mathbf{h}_k$. We emphasize that, for global noise, the SOI-induced rotation is independent of the location of the defects and affects noise and the Zeeman field in the same way. Local noise, on the other hand, locally rotates the noise fluctuators, yielding a qualitatively different effect compared to the Zeeman field.

This qualitative difference can be straightforwardly understood by considering a homogeneous SOI field, such as $\mathbf{v}_H$ in Eq. (41). In this case $\phi_s(z) = 0$ and we find that

$$\boldsymbol{\omega}_B = \tilde{\boldsymbol{\omega}}_B^\parallel + e^{-l^2/\lambda_s^2} \tilde{\boldsymbol{\omega}}_B^\perp \hat{R}_s^T(2\bar{z}/\lambda_s),$$
(C7a)

$$\tilde{\boldsymbol{H}}_G = \mathbf{h}^\parallel + e^{-l^2/\lambda_s^2} \mathbf{h}^\perp \hat{R}_s^T(2\bar{z}/\lambda_s),$$
(C7b)

$$\tilde{\boldsymbol{H}}_L = \frac{1}{n_0} \sum_k |\psi(z_k - \bar{z})|^2 \mathbf{h}_k \hat{R}_s^T[2z_k/\lambda_s],$$
(C7c)

where $\parallel$ and $\perp$ refer to components of the vectors parallel and perpendicular to the SOI $\mathbf{n}_s$, respectively.

We now focus on the case where the Zeeman field is perpendicular to the SOI, e.g., $\mathbf{n}_s = \mathbf{n}_1$ and $\tilde{\boldsymbol{\omega}}_B = \tilde{\omega}_B \mathbf{n}_3$. In the interaction picture including the dynamics induced by the Zeeman field, the relevant longitudinal noise is

$$[\tilde{\boldsymbol{H}}_G]_3 = e^{-l^2/\lambda_s^2} \mathbf{h} \cdot \mathbf{n}_3,$$
(C8a)

$$[\tilde{\boldsymbol{H}}_L]_3 = \frac{1}{n_0} \sum_k |\psi(z_k - \bar{z})|^2 \mathbf{h}_k \cdot \hat{R}_s^T[2(z_k - \bar{z})/\lambda_s] \mathbf{n}_3,$$
(C8b)

resulting in [see Eqs. (13) and (29)]

$$F_G = e^{-2l^2/\lambda_s^2} F_{FID} \quad \text{and} \quad F_L = F_P^L.$$
(C9)

APPENDIX D: EXACT RESULTS FOR THE FILTER FUNCTIONS

In this appendix, we report exact equations for the filter functions of a fully precessing Zeeman field and fidelities:

$$F_P = \frac{2[\omega_\lambda^2 - (\omega_\lambda^2 + \omega^2) \cos(t\omega) \cos(t\omega_\lambda) - 2\omega\omega_\lambda \sin(t\omega) \sin(t\omega_\lambda) + \omega^2]}{(\omega^2 - \omega_\lambda^2)^2},$$
(D1a)

$$\bar{\mathcal{F}}_P = \exp\left\{ \tfrac{1}{8} i\pi 2^{\eta-1} \csc(\pi\eta) t^{2-\eta} T^{\eta-2} [-(t\omega_\lambda + i)^{\eta-1} + (t\omega_\lambda - i)^{\eta-1} + (-t\omega_\lambda - i)^{\eta-1} - (-t\omega_\lambda + i)^{\eta-1}] \right\},$$
(D1b)

$$F_P^L = \frac{1}{\omega_l^2} \text{Re}\left[f\left(\frac{\omega - 2\omega_\lambda}{\omega_l}, \omega_l t \right) \right],$$
(D1c)

$$f(\omega, t) = e^{-(t^2 + \omega^2)/2} \left\{ \sqrt{\frac{2}{\pi}} e^{\omega^2/2} [\cos(t\omega) - e^{t^2/2}] + \frac{1}{2} e^{t^2/2} \left[(t + i\omega) \text{erf}\left(\frac{t + i\omega}{\sqrt{2}} \right) + (t - i\omega) \text{erf}\left(\frac{t - i\omega}{\sqrt{2}} \right) + 2\omega \text{erfi}\left(\frac{\omega}{\sqrt{2}} \right) \right] \right\}.$$
(D1d)

[1] S. G. J. Philips, M. T. Madzik, S. V. Amitonov, S. L. de Snoo, M. Russ, N. Kalhor, C. Volk, W. I. L. Lawrie, D. Brousse, L. Tryputen, B. P. Wuetz, A. Sammak, M. Veldhorst, G. Scappucci, and L. M. K. Vandersypen, Universal control of a six-qubit quantum processor in silicon, Nature **609**, 919 (2022).

[2] A. Noiri, K. Takeda, T. Nakajima, T. Kobayashi, A. Sammak, G. Scappucci, and S. Tarucha, Fast universal quantum gate above the fault-tolerance threshold in silicon, Nature **601**, 338 (2022).

[3] K. Takeda, A. Noiri, T. Nakajima, T. Kobayashi, and S. Tarucha, Quantum error correction with silicon spin qubits, Nature **608**, 682 (2022).

[4] X. Xue, M. Russ, N. Samkharadze, B. Undseth, A. Sammak, G. Scappucci, and L. M. K. Vandersypen, Quantum logic with spin qubits crossing the surface code threshold, Nature **601**, 343 (2022).

[5] D. M. Zajac, A. J. Sigillito, M. Russ, F. Borjans, J. M. Taylor, G. Burkard, and J. R. Petta, Resonantly driven CNOT gate for electron spins, Science **359**, 439 (2018).

[6] N. W. Hendrickx, W. I. L. Lawrie, M. Russ, F. van Riggelen, S. L. de Snoo, R. N. Schouten, A. Sammak, G. Scappucci, and M. Veldhorst, A four-qubit germanium quantum processor, Nature **591**, 580 (2021).

[7] N. Hendrickx, D. Franke, A. Sammak, G. Scappucci, and M. Veldhorst, Fast two-qubit logic with holes in germanium, Nature **577**, 487 (2020).

[8] H. Watzinger, J. Kukučka, L. Vukušić, F. Gao, T. Wang, F. Schäffler, J.-J. Zhang, and G. Katsaros, A germanium hole spin qubit, Nat. Commun. **9**, 3902 (2018).

[9] D. Jirovec, A. Hofmann, A. Ballabio, P. M. Mutter, G. Tavani, M. Botifoll, A. Crippa, J. Kukucka, O. Sagi, F. Martins, J. Saez-Mollejo, I. Prieto, M. Borovkov, J. Arbiol, D. Chrastina, G. Isella, and G. Katsaros, A singlet-triplet hole spin qubit in planar Ge, Nat. Mater. **20**, 1106 (2021).

[10] S. Liles, D. Halverson, Z. Wang, A. Shamim, R. Eggli, I. Jin, J. Hillier, K. Kumar, I. Vorreiter, M. Rendell, J. H. Huang, C. C. Escott, F. E. Hudson, W. H. Lim, D. Culcer, A. S. Dzurak, and A. R. Hamilton, A singlet-triplet hole-spin qubit in MOS silicon, ArXiv:2310.09722.

[11] A. R. Mills, C. R. Guinn, M. J. Gullans, A. J. Sigillito, M. M. Feldman, E. Nielsen, and J. R. Petta, Two-qubit silicon quantum processor with operation fidelity exceeding 99%, Sci. Adv. **8**, eabn5130 (2022).

[12] C. Kloeffel and D. Loss, Prospects for spin-based quantum computing in quantum dots, Annu. Rev. Condens. Matter Phys. **4**, 51 (2013).

[13] G. Burkard, T. D. Ladd, A. Pan, J. M. Nichol, and J. R. Petta, Semiconductor spin qubits, Rev. Mod. Phys. **95**, 025003 (2023).

[14] G. Scappucci, C. Kloeffel, F. A. Zwanenburg, D. Loss, M. Myronov, J.-J. Zhang, S. De Franceschi, G. Katsaros, and M. Veldhorst, The germanium quantum information route, Nat. Rev. Mater. **6**, 926 (2021).

[15] S. Geyer, B. Hetényi, S. Bosco, L. C. Camenzind, R. S. Eggli, A. Fuhrer, D. Loss, R. J. Warburton, D. M. Zumbühl, and A. V. Kuhlmann, Anisotropic exchange interaction of two hole-spin qubits, Nat. Phys. (2024).

[16] A. M. J. Zwerver, *et al.*, Qubits made by advanced semiconductor manufacturing, Nat. Electron. **5**, 184 (2022).

[17] R. Maurand, X. Jehl, D. Kotekar-Patil, A. Corna, H. Bohuslavskyi, R. Laviéville, L. Hutin, S. Barraud, M. Vinet, M. Sanquer, and S. De Franceschi, A CMOS silicon spin qubit, Nat. Commun. **7**, 1 (2016).

[18] L. C. Camenzind, S. Geyer, A. Fuhrer, R. J. Warburton, D. M. Zumbühl, and A. V. Kuhlmann, A hole spin qubit in a fin field-effect transistor above 4 kelvin, Nat. Electron. **5**, 178 (2022).

[19] L. Petit, J. M. Boter, H. G. J. Eenink, G. Droulers, M. L. V. Tagliaferri, R. Li, D. P. Franke, K. J. Singh, J. S. Clarke, R. N. Schouten, V. V. Dobrovitski, L. M. K. Vandersypen, and M. Veldhorst, Spin lifetime and charge noise in hot silicon quantum dot qubits, Phys. Rev. Lett. **121**, 076801 (2018).

[20] C. H. Yang, R. C. C. Leon, J. C. C. Hwang, A. Saraiva, T. Tanttu, W. Huang, J. Camirand Lemyre, K. W. Chan, K. Y. Tan, F. E. Hudson, K. M. Itoh, A. Morello, M. Pioro-Ladrière, A. Laucht, and A. S. Dzurak, Operation of a silicon quantum processor unit cell above one kelvin, Nature **580**, 350 (2020).

[21] L. Petit, H. G. J. Eenink, M. Russ, W. I. L. Lawrie, N. W. Hendrickx, S. G. J. Philips, J. S. Clarke, L. M. K. Vandersypen, and M. Veldhorst, Universal quantum logic in hot silicon qubits, Nature **580**, 355 (2020).

[22] B. Undseth, O. Pietx-Casas, E. Raymenants, M. Mehmandoost, M. T. Mądzik, S. G. J. Philips, S. L. de Snoo, D. J. Michalak, S. V. Amitonov, L. Tryputen, B. P. Wuetz, V. Fezzi, D. D. Esposti, A. Sammak, G. Scappucci, and L. M. K. Vandersypen, Hotter is easier: Unexpected temperature dependence of spin qubit frequencies, Phys. Rev. X **13**, 041015 (2023).

[23] L. M. K. Vandersypen, H. Bluhm, J. S. Clarke, A. S. Dzurak, R. Ishihara, A. Morello, D. J. Reilly, L. R. Schreiber, and M. Veldhorst, Interfacing spin qubits in quantum dots and donors—hot, dense, and coherent, npj Quantum Inf. **3**, 34 (2017).

[24] X. Xue, *et al.*, CMOS-based cryogenic control of silicon quantum circuits, Nature **593**, 205 (2021).

[25] J. M. Boter, J. P. Dehollain, J. P. van Dijk, Y. Xu, T. Hensgens, R. Versluis, H. W. Naus, J. S. Clarke, M. Veldhorst, F. Sebastiano, and L. M. Vandersypen, Spiderweb array: A sparse spin-qubit array, Phys. Rev. Appl. **18**, 024053 (2022).

[26] P. L. Bavdaz, H. G. J. Eenink, J. van Staveren, M. Lodari, C. G. Almudever, J. S. Clarke, F. Sebasatiano, M. Veldhorst, and G. Scappucci, A quantum dot cross-bar with sublinear scaling of interconnects at cryogenic temperature, npj Quantum Inf. **8**, 86 (2022).

[27] M. F. Gonzalez-Zalba, S. de Franceschi, E. Charbon, T. Meunier, M. Vinet, and A. S. Dzurak, Scaling silicon-based quantum computing using CMOS technology, Nat. Electron. **4**, 872 (2021).

[28] M. Künne, A. Willmes, M. Oberländer, C. Gorjaew, J. D. Teske, H. Bhardwaj, M. Beer, E. Kammerloher, R. Otten, I. Seidler, R. Xue, L. R. Schreiber, and H. Bluhm, The spinbus architecture: Scaling spin qubits with electron shuttling, ArXiv:2306.16348.

[29] M. Veldhorst, H. G. J. Eenink, C. H. Yang, and A. S. Dzurak, Silicon CMOS architecture for a spin-based quantum computer, Nat. Commun. **8**, 1766 (2017).

[30] R. Li, L. Petit, D. P. Franke, J. P. Dehollain, J. Helsen, M. Steudtner, N. K. Thomas, Z. R. Yoscovits, K. J. Singh, S. Wehner, L. M. K. Vandersypen, J. S. Clarke, and M. Veldhorst, A crossbar network for silicon quantum dot qubits, Sci. Adv. **4**, eaar3960 (2018).

[31] F. Borsoi, N. W. Hendrickx, V. John, M. Meyer, S. Motz, F. van Riggelen, A. Sammak, S. L. de Snoo, G. Scappucci, and M. Veldhorst, Shared control of a 16 semiconductor quantum dot crossbar array, Nat. Nanotechnol. **19**, 21 (2023).

[32] V. John, F. Borsoi, Z. György, C.-A. Wang, G. Széchenyi, F. van Riggelen-Doelman, W. I. L. Lawrie, N. W. Hendrickx, A. Sammak, G. Scappucci, A. Pályi, and M. Veldhorst, Bichromatic Rabi control of semiconductor qubits, Phys. Rev. Lett. **132**, 067001 (2024).

[33] X. Mi, M. Benito, S. Putz, D. M. Zajac, J. M. Taylor, G. Burkard, and J. R. Petta, A coherent spin–photon interface in silicon, Nature **555**, 599 (2018).

[34] A. J. Landig, J. V. Koski, P. Scarlino, U. C. Mendes, A. Blais, C. Reichl, W. Wegscheider, A. Wallraff, K. Ensslin, and T. Ihn, Coherent spin–photon coupling using a resonant exchange qubit, Nature **560**, 179 (2018).

[35] J. J. Viennot, M. C. Dartiailh, A. Cottet, and T. Kontos, Coherent coupling of a single spin to microwave cavity photons, Science **349**, 408 (2015).

[36] C. X. Yu, S. Zihlmann, J. C. Abadillo-Uriel, V. P. Michal, N. Rambal, H. Niebojewski, T. Bedecarrats, M. Vinet, É. Dumur, M. Filippone, B. Bertrand, S. De Franceschi, Y.-M. Niquet, and R. Maurand, Strong coupling between a photon and a hole spin in silicon, Nat. Nanotechnol. **18**, 741 (2023).

[37] P. Harvey-Collard, J. Dijkema, G. Zheng, A. Sammak, G. Scappucci, and L. M. K. Vandersypen, Coherent spin-spin coupling mediated by virtual microwave photons, Phys. Rev. X **12**, 021026 (2022).

[38] T. Bonsen, P. Harvey-Collard, M. Russ, J. Dijkema, A. Sammak, G. Scappucci, and L. M. K. Vandersypen, Probing the Jaynes-Cummings ladder with spin circuit quantum electrodynamics, Phys. Rev. Lett. **130**, 137001 (2023).

[39] P.-Q. Jin, M. Marthaler, A. Shnirman, and G. Schön, Strong coupling of spin qubits to a transmission line resonator, Phys. Rev. Lett. **108**, 190506 (2012).

[40] S. Bosco, P. Scarlino, J. Klinovaja, and D. Loss, Fully tunable longitudinal spin-photon interactions in Si and Ge quantum dots, Phys. Rev. Lett. **129**, 066801 (2022).

[41] S. E. Nigg, A. Fuhrer, and D. Loss, Superconducting grid-bus surface code architecture for hole-spin qubits, Phys. Rev. Lett. **118**, 147701 (2017).

[42] A. Warren, E. Barnes, and S. E. Economou, Long-distance entangling gates between quantum dot spins mediated by a superconducting resonator, Phys. Rev. B **100**, 161303 (2019).

[43] M. Benito, J. R. Petta, and G. Burkard, Optimized cavity-mediated dispersive two-qubit gates between spin qubits, Phys. Rev. B **100**, 081412 (2019).

[44] M. Benito, X. Mi, J. M. Taylor, J. R. Petta, and G. Burkard, Input-output theory for spin-photon coupling in Si double quantum dots, Phys. Rev. B **96**, 235434 (2017).

[45] C. Kloeffel, M. Trif, P. Stano, and D. Loss, Circuit QED with hole-spin qubits in Ge/Si nanowire quantum dots, Phys. Rev. B **88**, 241405 (2013).

[46] P. M. Mutter and G. Burkard, Natural heavy-hole flopping mode qubit in germanium, Phys. Rev. Res. **3**, 013194 (2021).

[47] T. Cubaynes, M. R. Delbecq, M. C. Dartiailh, R. Assouly, M. M. Desjardins, L. C. Contamin, L. E. Bruhat, Z. Leghtas, F. Mallet, A. Cottet, and T. Kontos, Highly coherent spin states in carbon nanotubes coupled to cavity photons, npj Quantum Inf. **5**, 47 (2019).

[48] F. Borjans, X. G. Croot, X. Mi, M. J. Gullans, and J. R. Petta, Resonant microwave-mediated interactions between distant electron spins, Nature **577**, 195 (2020).

[49] F. De Palma, F. Oppliger, W. Jang, S. Bosco, M. Janík, S. Calcaterra, G. Katsaros, G. Isella, D. Loss, and P. Scarlino, Strong hole-photon coupling in planar Ge: Probing the charge degree and wigner molecule states, ArXiv:2310.20661.

[50] J. J. Viennot, J. Palomo, and T. Kontos, Stamping single wall nanotubes for circuit quantum electrodynamics, Appl. Phys. Lett. **104**, 113108 (2014).

[51] T. M. Stace, C. H. W. Barnes, and G. J. Milburn, Mesoscopic one-way channels for quantum state transfer via the quantum Hall effect, Phys. Rev. Lett. **93**, 126804 (2004).

[52] S. Bosco and D. P. DiVincenzo, Transmission lines and resonators based on quantum hall plasmonics: Electromagnetic field, attenuation, and coupling to qubits, Phys. Rev. B **100**, 035416 (2019).

[53] S. J. Elman, S. D. Bartlett, and A. C. Doherty, Long-range entanglement for spin qubits via quantum Hall edge modes, Phys. Rev. B **96**, 115407 (2017).

[54] S. Bosco, D. DiVincenzo, and D. Reilly, Transmission lines and metamaterials based on quantum Hall plasmonics, Phys. Rev. Appl. **12**, 014030 (2019).

[55] G. Yang, C.-H. Hsu, P. Stano, J. Klinovaja, and D. Loss, Long-distance entanglement of spin qubits via quantum Hall edge states, Phys. Rev. B **93**, 075301 (2016).

[56] L. Trifunovic, O. Dial, M. Trif, J. R. Wootton, R. Abebe, A. Yacoby, and D. Loss, Long-distance spin-spin coupling via floating gates, Phys. Rev. X **2**, 011006 (2012).

[57] M. Serina, C. Kloeffel, and D. Loss, Long-range interaction between charge and spin qubits in quantum dots, Phys. Rev. B **95**, 245422 (2017).

[58] L. Trifunovic, F. L. Pedrocchi, and D. Loss, Long-distance entanglement of spin qubits via ferromagnet, Phys. Rev. X **3**, 041023 (2013).

[59] M. Fukami, D. R. Candido, D. D. Awschalom, and M. E. Flatté, Opportunities for long-range magnon-mediated entanglement of spin qubits via on- and off-resonant coupling, PRX Quantum **2**, 040314 (2021).

[60] B. Flebus and Y. Tserkovnyak, Entangling distant spin qubits via a magnetic domain wall, Phys. Rev. B **99**, 140403 (2019).

[61] W. Xiong, M. Tian, G.-Q. Zhang, and J. Q. You, Strong long-range spin-spin coupling via a Kerr magnon interface, Phys. Rev. B **105**, 245310 (2022).

[62] J. Zou, S. Bosco, B. Pal, S. S. P. Parkin, J. Klinovaja, and D. Loss, Quantum computing on magnetic racetracks with flying domain wall qubits, Phys. Rev. Res. **5**, 033166 (2023).

[63] B. Hetényi, A. Mook, J. Klinovaja, and D. Loss, Long-distance coupling of spin qubits via topological magnons, Phys. Rev. B **106**, 235409 (2022).

[64] J. Zou, S. Zhang, and Y. Tserkovnyak, Bell-state generation for spin qubits via dissipative coupling, Phys. Rev. B **106**, L180406 (2022).

[65] J. Zou, S. Bosco, and D. Loss, Spatially correlated classical and quantum noise in driven qubits, npj Quantum Inf. **10**, 46 (2024).

[66] A. Zwerver, S. Amitonov, S. de Snoo, M. Mądzik, M. Rimbach-Russ, A. Sammak, G. Scappucci, and L. Vandersypen, Shuttling an electron spin through a silicon quantum dot array, PRX Quantum **4**, 030303 (2023).

[67] J. Yoneda, W. Huang, M. Feng, C. H. Yang, K. W. Chan, T. Tanttu, W. Gilbert, R. C. C. Leon, F. E. Hudson, K. M. Itoh, A. Morello, S. D. Bartlett, A. Laucht, A. Saraiva, and A. S. Dzurak, Coherent spin qubit transport in silicon, Nat. Commun. **12**, 4114 (2021).

[68] A. R. Mills, D. M. Zajac, M. J. Gullans, F. J. Schupp, T. M. Hazard, and J. R. Petta, Shuttling a single charge across a one-dimensional array of silicon quantum dots, Nat. Commun. **10**, 1063 (2019).

[69] T. Fujita, T. A. Baart, C. Reichl, W. Wegscheider, and L. M. K. Vandersypen, Coherent shuttle of electron-spin states, npj Quantum Inf. **3**, 22 (2017).

[70] F. van Riggelen-Doelman, C.-A. Wang, S. L. de Snoo, W. I. Lawrie, N. W. Hendrickx, M. Rimbach-Russ, A. Sammak, G. Scappucci, C. Déprez, and M. Veldhorst, Coherent spin qubit shuttling through germanium quantum dots, ArXiv:2308.02406.

[71] I. Seidler, T. Struck, R. Xue, N. Focke, S. Trellenkamp, H. Bluhm, and L. R. Schreiber, Conveyor-mode single-electron shuttling in Si/SiGe for a scalable quantum computing architecture, npj Quantum Inf. **8**, 100 (2022).

[72] T. Struck, M. Volmer, L. Visser, T. Offermann, R. Xue, J.-S. Tu, S. Trellenkamp, Ł. Cywiński, H. Bluhm, and L. R. Schreiber, Spin-EPR-pair separation by conveyor-mode single electron shuttling in Si/SiGe, Nat. Commun. **15**, 1325 (2024).

[73] V. Langrock, J. A. Krzywda, N. Focke, I. Seidler, L. R. Schreiber, and L. Cywiński, Blueprint of a scalable spin qubit shuttle device for coherent mid-range qubit transfer in disordered Si/SiGe/SiO$_2$, PRX Quantum **4**, 020305 (2023).

[74] C. Kloeffel, M. Trif, and D. Loss, Strong spin-orbit interaction and helical hole states in Ge/Si nanowires, Phys. Rev. B **84**, 195314 (2011).

[75] C. Kloeffel, M. J. Rancic, and D. Loss, Direct Rashba spin-orbit interaction in Si and Ge nanowires with different growth directions, Phys. Rev. B **97**, 235422 (2018).

[76] F. N. M. Froning, L. C. Camenzind, O. A. H. van der Molen, A. Li, E. P. A. M. Bakkers, D. M. Zumbühl, and F. R. Braakman, Ultrafast hole spin qubit with gate-tunable spin–orbit switch functionality, Nat. Nanotechnol. **16**, 308 (2021).

[77] K. Wang, G. Xu, F. Gao, H. Liu, R.-L. Ma, X. Zhang, Z. Wang, G. Cao, T. Wang, J.-J. Zhang, D. Culcer, X. Hu, H.-W. Jiang, H.-O. Li, G.-C. Guo, and G.-P. Guo, Ultra-fast coherent control of a hole spin qubit in a germanium quantum dot, Nat. Commun. **13**, 206 (2022).

[78] F. N. M. Froning, M. J. Rančić, B. Hetényi, S. Bosco, M. K. Rehmann, A. Li, E. P. A. M. Bakkers, F. A. Zwanenburg, D. Loss, D. M. Zumbühl, and F. R. Braakman, Strong spin-orbit interaction and g-factor renormalization of hole spins in Ge/Si nanowire quantum dots, Phys. Rev. Res. **3**, 013081 (2021).

[79] H. Liu, K. Wang, F. Gao, J. Leng, Y. Liu, Y.-C. Zhou, G. Cao, T. Wang, J. Zhang, P. Huang, H.-O. Li, and G.-P. Guo, Ultrafast and electrically tunable Rabi frequency in a germanium hut wire hole spin qubit, Nano Lett. **23**, 3810 (2023).

[80] L. A. Terrazos, E. Marcellina, Z. Wang, S. N. Coppersmith, M. Friesen, A. R. Hamilton, X. Hu, B. Koiller, A. L. Saraiva, D. Culcer, and R. B. Capaz, Theory of hole-spin qubits in strained germanium quantum dots, Phys. Rev. B **103**, 125201 (2021).

[81] S. Bosco, M. Benito, C. Adelsberger, and D. Loss, Squeezed hole spin qubits in Ge quantum dots with ultrafast gates at low power, Phys. Rev. B **104**, 115425 (2021).

[82] C. Adelsberger, M. Benito, S. Bosco, J. Klinovaja, and D. Loss, Hole-spin qubits in Ge nanowire quantum dots: Interplay of orbital magnetic field, strain, and growth direction, Phys. Rev. B **105**, 075308 (2022).

[83] C. Adelsberger, S. Bosco, J. Klinovaja, and D. Loss, Enhanced orbital magnetic field effects in Ge hole nanowires, Phys. Rev. B **106**, 235408 (2022).

[84] J. C. Abadillo-Uriel, E. A. Rodríguez-Mena, B. Martinez, and Y.-M. Niquet, Hole-spin driving by strain-induced spin-orbit interactions, Phys. Rev. Lett. **131**, 097002 (2023).

[85] B. Martinez, J. C. Abadillo-Uriel, E. A. Rodríguez-Mena, and Y.-M. Niquet, Hole spin manipulation in inhomogeneous and nonseparable electric fields, Phys. Rev. B **106**, 235426 (2022).

[86] S. Bosco, S. Geyer, L. C. Camenzind, R. S. Eggli, A. Fuhrer, R. J. Warburton, D. M. Zumbühl, J. C. Egues, A. V. Kuhlmann, and D. Loss, Phase-driving hole spin qubits, Phys. Rev. Lett. **131**, 197001 (2023).

[87] A. Sarkar, Z. Wang, M. Rendell, N. W. Hendrickx, M. Veldhorst, G. Scappucci, M. Khalifa, J. Salfi, A. Saraiva, A. S. Dzurak, A. R. Hamilton, and D. Culcer, Electrical operation of planar Ge hole spin qubits in an in-plane magnetic field, Phys. Rev. B **108**, 245301 (2023).

[88] S. Bosco, B. Hetényi, and D. Loss, Hole spin qubits in Si FinFETs with fully tunable spin-orbit coupling and sweet spots for charge noise, PRX Quantum **2**, 010348 (2021).

[89] S. Bosco and D. Loss, Fully tunable hyperfine interactions of hole spin qubits in Si and Ge quantum dots, Phys. Rev. Lett. **127**, 190501 (2021).

[90] N. Piot, B. Brun, V. Schmitt, S. Zihlmann, V. P. Michal, A. Apra, J. C. Abadillo-Uriel, X. Jehl, B. Bertrand, H. Niebojewski, L. Hutin, M. Vinet, M. Urdampilleta, T. Meunier, Y.-M. Niquet, R. Maurand, and S. D. Franceschi, A single hole spin with enhanced coherence in natural silicon, Nat. Nanotechnol. **17**, 1072 (2022).

[91] S. Bosco and D. Loss, Hole spin qubits in thin curved quantum wells, Phys. Rev. Appl. **18**, 044038 (2022).

[92] C.-A. Wang, G. Scappucci, M. Veldhorst, and M. Russ, Modelling of planar germanium hole qubits in electric and magnetic fields, ArXiv:2208.04795.

[93] V. P. Michal, J. C. Abadillo-Uriel, S. Zihlmann, R. Maurand, Y.-M. Niquet, and M. Filippone, Tunable hole spin-photon interaction based on g-matrix modulation, Phys. Rev. B **107**, L041303 (2023).

[94] Z. Wang, E. Marcellina, A. R. Hamilton, J. H. Cullen, S. Rogge, J. Salfi, and D. Culcer, Optimal operation points for ultrafast, highly coherent Ge hole spin-orbit qubits, npj Quantum Inf. **7**, 54 (2021).

[95] N. Hendrickx, L. Massai, M. Mergenthaler, F. Schupp, S. Paredes, S. Bedell, G. Salis, and A. Fuhrer, Sweet-spot operation of a germanium hole spin qubit with highly anisotropic noise sensitivity, Nat. Mater. (2024).

[96] L. Cywiński, R. M. Lutchyn, C. P. Nave, and S. Das Sarma, How to enhance dephasing time in superconducting qubits, Phys. Rev. B **77**, 174509 (2008).

[97] A. Crippa, R. Maurand, L. Bourdet, D. Kotekar-Patil, A. Amisse, X. Jehl, M. Sanquer, R. Laviéville, H. Bohuslavskyi, L. Hutin, S. Barraud, M. Vinet, Y.-M. Niquet, and S. De Franceschi, Electrical spin driving by g-matrix modulation in spin-orbit qubits, Phys. Rev. Lett. **120**, 137702 (2018).

[98] S. D. Liles, F. Martins, D. S. Miserev, A. A. Kiselev, I. D. Thorvaldson, M. J. Rendell, I. K. Jin, F. E. Hudson, M. Veldhorst, K. M. Itoh, O. P. Sushkov, T. D. Ladd, A. S. Dzurak, and A. R. Hamilton, Electrical control of the g tensor of the first hole in a silicon MOS quantum dot, Phys. Rev. B **104**, 235303 (2021).

[99] M. Aldeghi, R. Allenspach, and G. Salis, Modular nanomagnet design for spin qubits confined in a linear chain, Appl. Phys. Lett. **122**, 134003 (2023).

[100] J. A. Krzywda and L. Cywiński, Interplay of charge noise and coupling to phonons in adiabatic electron transfer between quantum dots, Phys. Rev. B **104**, 075439 (2021).

[101] P. Del Vecchio and O. Moutanabbir, Light-hole gate-defined spin-orbit qubit, Phys. Rev. B **107**, L161406 (2023).

[102] J.-X. Xiong, S. Guan, J.-W. Luo, and S.-S. Li, Emergence of strong tunable linear Rashba spin-orbit coupling in two-dimensional hole gases in semiconductor quantum wells, Phys. Rev. B **103**, 085309 (2021).

[103] E. A. Rodríguez-Mena, J. C. Abadillo-Uriel, G. Veste, B. Martinez, J. Li, B. Sklénard, and Y.-M. Niquet, Linear-in-momentum spin orbit interactions in planar Ge/GeSi heterostructures and spin qubits, Phys. Rev. B **108**, 205416 (2023).

[104] S. Assali, A. Attiaoui, P. D. Vecchio, S. Mukherjee, J. Nicolas, and O. Moutanabbir, A light-hole germanium quantum well on silicon, Adv. Mater. **34**, 2201192 (2022).

[105] J. D. Cifuentes, et al., Bounds to electron spin qubit variability for scalable CMOS architectures, Nat. Commun. **15**, 4299 (2024).

[106] D. Degli Esposti, L. E. A. Stehouwer, Ö. Gül, N. Samkharadze, C. Déprez, M. Meyer, I. N. Meijer, L. Tryputen, S. Karwal, M. Botifoll, J. Arbiol, S. V. Amitonov, L. M. K. Vandersypen, A. Sammak, M. Veldhorst, and G. Scappucci, Low disorder and high valley splitting in silicon, npj Quantum Inf. **10**, 32 (2024).

[107] D. Jirovec, P. M. Mutter, A. Hofmann, A. Crippa, M. Rychetsky, D. L. Craig, J. Kukucka, F. Martins, A. Ballabio, N. Ares, D. Chrastina, G. Isella, G. Burkard, and G. Katsaros, Dynamics of hole singlet-triplet qubits with large g-factor differences, Phys. Rev. Lett. **128**, 126803 (2022).

[108] L. Viola and E. Knill, Random decoupling schemes for quantum dynamical control and error suppression, Phys. Rev. Lett. **94**, 060502 (2005).

[109] O. Kern and G. Alber, Controlling quantum systems by embedded dynamical decoupling schemes, Phys. Rev. Lett. **95**, 250501 (2005).

[110] L. F. Santos and L. Viola, Enhanced convergence and robust performance of randomized dynamical decoupling, Phys. Rev. Lett. **97**, 150501 (2006).

[111] J. Fischer, W. A. Coish, D. V. Bulaev, and D. Loss, Spin decoherence of a heavy hole coupled to nuclear spins in a quantum dot, Phys. Rev. B **78**, 155329 (2008).

[112] J. Fischer and D. Loss, Hybridization and spin decoherence in heavy-hole quantum dots, Phys. Rev. Lett. **105**, 266603 (2010).

[113] J. Yoneda, K. Takeda, T. Otsuka, T. Nakajima, M. R. Delbecq, G. Allison, T. Honda, T. Kodera, S. Oda, Y. Hoshi, N. Usami, K. M. Itoh, and S. Tarucha, A quantum-dot spin qubit with coherence limited by charge noise and fidelity higher than 99.9%, Nat. Nanotechnol. **13**, 102 (2018).

[114] T. Struck, A. Hollmann, F. Schauer, O. Fedorets, A. Schmidbauer, K. Sawano, H. Riemann, N. V. Abrosimov, Ł. Cywiński, D. Bougeard, and L. R. Schreiber, Low-frequency spin qubit energy splitting noise in highly purified ^{28}Si/SiGe, npj Quantum Inf. **6**, 40 (2020).

[115] To derive Eq. (11), we used $[R_Z^T(\tau)R_Z(\tau')]_{33} = [R_B^T(\tau) R_B(\tau')]_{33} = [R_B(\tau)\mathbf{n}_3] \cdot [R_B(\tau')\mathbf{n}_3] = \boldsymbol{\omega}_B[\bar{z}(\tau)] \cdot \boldsymbol{\omega}_B [\bar{z}(\tau')]/|\boldsymbol{\omega}_B[\bar{z}(\tau)]||\boldsymbol{\omega}_B[\bar{z}(\tau')]|$.

[116] Y. Makhlin, G. Schön, and A. Shnirman, Dissipative effects in Josephson qubits, Chem. Phys. **296**, 315 (2004), the Spin-Boson Problem: From Electron Transfer to Quantum Computing . . . to the 60th Birthday of Professor Ulrich Weiss.

[117] P. Philippopoulos, S. Chesi, and W. A. Coish, First-principles hyperfine tensors for electrons and holes in GaAs and silicon, Phys. Rev. B **101**, 115302 (2020).

[118] P. Huang and X. Hu, Spin qubit relaxation in a moving quantum dot, Phys. Rev. B **88**, 075301 (2013).

[119] D. Zeuch, F. Hassler, J. J. Slim, and D. P. DiVincenzo, Exact rotating wave approximation, Ann. Phys. (N. Y.) **423**, 168327 (2020).

[120] A. Laucht, R. Kalra, S. Simmons, J. P. Dehollain, J. T. Muhonen, F. A. Mohiyaddin, S. Freer, F. E. Hudson, K. M. Itoh, D. N. Jamieson, J. C. McCallum, A. S. Dzurak, and A. Morello, A dressed spin qubit in silicon, Nat. Nanotechnol. **12**, 61 (2017).

[121] A. E. Seedhouse, I. Hansen, A. Laucht, C. H. Yang, A. S. Dzurak, and A. Saraiva, Quantum computation protocol for dressed spins in a global field, Phys. Rev. B **104**, 235411 (2021).

[122] I. Hansen, A. E. Seedhouse, K. W. Chan, F. E. Hudson, K. M. Itoh, A. Laucht, A. Saraiva, C. H. Yang, and A. S.

Dzurak, Implementation of an advanced dressing protocol for global qubit control in silicon, Appl. Phys. Rev. **9**, 031409 (2022).

[123] Y.-C. Yang, S. N. Coppersmith, and M. Friesen, Achieving high-fidelity single-qubit gates in a strongly driven charge qubit with $1/f$ charge noise, npj Quantum Inf. **5**, 12 (2019).

[124] Y.-C. Yang, S. N. Coppersmith, and M. Friesen, High-fidelity single-qubit gates in a strongly driven quantum-dot hybrid qubit with $1/f$ charge noise, Phys. Rev. A **100**, 022337 (2019).

[125] D. Fernández-Fernández, Y. Ban, and G. Platero, Quantum control of hole spin qubits in double quantum dots, Phys. Rev. Appl. **18**, 054090 (2022).

[126] M. Rimbach-Russ, S. G. Philips, X. Xue, and L. M. Vandersypen, Simple framework for systematic high-fidelity gate operations, Quantum Sci. Technol. **8**, 045025 (2023).